Journal of Medicinal Chemistry

pubs.acs.org/jmc

Article

Optimization of Artificial Siderophores as ^{68}Ga-Complexed PET Tracers for In Vivo Imaging of Bacterial Infections

Carsten Peukert, Laura N. B. Langer, Sophie M. Wegener, Anna Tutov, Jens P. Bankstahl, Bianka Karge, Frank M. Bengel, Tobias L. Ross,* and Mark Brönstrup*

Cite This: *J. Med. Chem.* 2021, 64, 12359–12378

Read Online

ACCESS | Metrics & More | Article Recommendations | Supporting Information

ABSTRACT: The diagnosis of bacterial infections at deep body sites benefits from noninvasive imaging of molecular probes that can be traced by positron emission tomography (PET). We specifically labeled bacteria by targeting their iron transport system with artificial siderophores. The cyclen-based probes contain different binding sites for iron and the PET nuclide gallium-68. A panel of 11 siderophores with different iron coordination numbers and geometries was synthesized in up to 8 steps, and candidates with the best siderophore potential were selected by a growth recovery assay. The probes [^{68}Ga]**7** and [^{68}Ga]**15** were found to be suitable for PET imaging based on their radiochemical yield, radiochemical purity, and complex stability in vitro and in vivo. Both showed significant uptake in mice infected with *Escherichia coli* and were able to discern infection from lipopolysaccharide-triggered, sterile inflammation. The study qualifies cyclen-based artificial siderophores as readily accessible scaffolds for the in vivo imaging of bacteria.

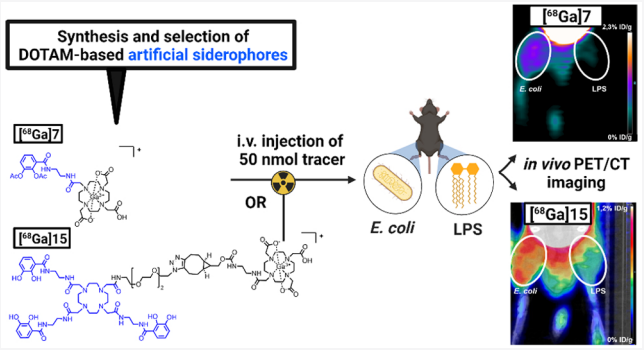

INTRODUCTION

Infections with pathogenic bacteria are a cause of high morbidity and mortality and therefore constitute a major threat for human health.[1] This situation is exacerbated by the rise of antimicrobial resistance, rendering established treatments ineffective, while the pipeline of novel, resistance-breaking antibiotics remains thin.[2,3] Today's diagnosis of bacterial infections is based on clinical symptoms and the analysis of biofluids, typically blood or urine, using microbiological, genetic, and mass spectrometric techniques. However, the analysis of biofluids struggles to detect early-stage infections at deep body sites (e.g., heart, brain, or medical implants) that are hardly accessible for sampling. For such cases, noninvasive imaging techniques with molecular probes that localize bacterial infections bear the potential to improve diagnostic capabilities significantly, as outlined by recent reviews in this and other journals.[4−6] In fact, infection imaging of vulnerable patient populations (e.g., following cancer chemotherapy or organ transplantation) has already become clinical practice, and it is mostly based on the detection of [^{18}F]fluorodeoxyglucose (FDG) by positron emission tomography (PET). Because FDG is taken up by all metabolically active cells, the tracer has low specificity and cannot distinguish between sterile inflammation and infection.[7,8] Therefore, some alternative approaches to identify bacteria-specific PET tracers have been pursued recently. For example, white blood cells or antibodies could be labeled ^{67}Ga, ^{99m}Tc, or ^{111}In and have been successfully applied in the imaging of osteomyelitis or prosthetic joint infections.[9] One strategy is to employ ^{18}F-labeled carbohydrates that are internalized by transporters not expressed in eukaryotes.[10−19] Also, essential bacterial metabolites have been converted to radioactive imaging probes.[20] In a different approach, antibiotic drugs or human antimicrobial defense peptides served as the scaffold for PET-probes.[21−24] Recently, D-[5-^{11}C]glutamine could specifically discriminate live *Escherichia coli* and *MRSA* in dual-infection murine myositis model versus sterile inflammation caused by heat-killed bacteria.[25]

A third strategy, pursued in this study, is to utilize the active iron transport systems of bacteria for a selective and pronounced uptake of the probe. To cover their continued demand for iron ions, bacteria synthetize small molecular weight iron chelators, the so-called siderophores (*greek: sidero = iron* and *phoros = carrier*), that are secreted to the environment and actively internalized by bacterial outer membrane receptors, once loaded with iron.[26] Because Ga^{3+} ions exhibit similar coordination properties to Fe^{3+} ions,

Received: June 11, 2021
Published: August 9, 2021

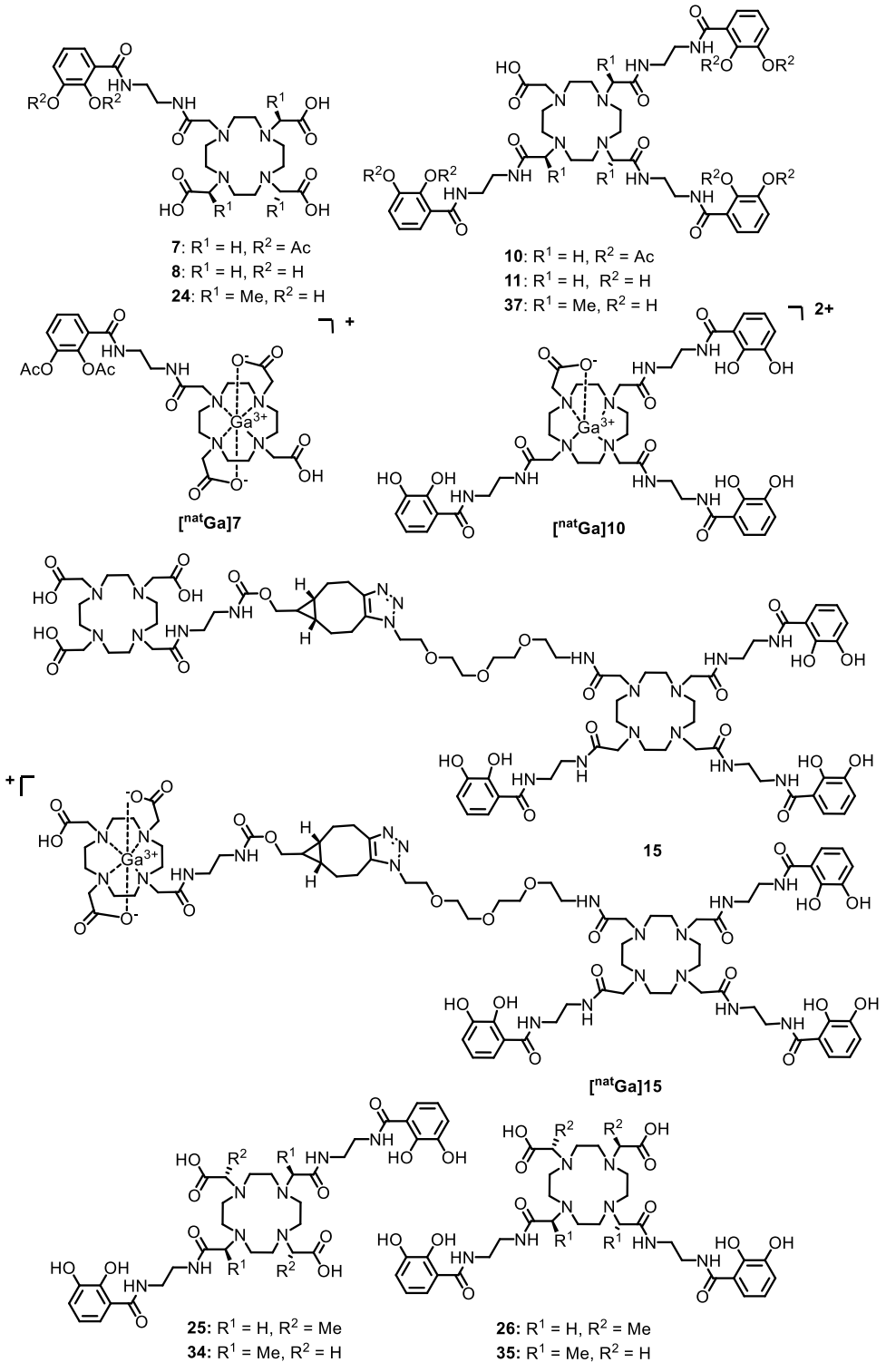

Figure 1. Structures of artificial siderophores investigated in this study.

siderophore-based imaging probes have been proposed, which are loaded with the positron emitter gallium-68 instead of iron.[4] First, in vivo studies have been conducted to image the fungus *Aspergillus fumigatus* with [^{68}Ga]triacetyl fusarine and ferrioxamine derivatives,[27,28] or *Pseudomonas aeruginosa* with gallium-68 complexed pyoverdine.[29] Lately, a ^{68}Ga-labeled version of the clinically used antidote desferrioxamine (Desferal, DFO-B) has been repurposed in an acute murine myositis model to image Gram-positive and Gram-negative bacteria in vivo.[30] Of note, siderophores have been widely employed as Trojan horses, transporting a broad range of payloads efficiently into bacterial cells.[31] The success of this concept has been underlined by the approval of the first siderophore-coupled antibiotic cefiderocol (Fetroja) in 2019.[32] While the above-mentioned studies use the iron binding site of a natural siderophore to incorporate the PET tracer, we envisaged to (i) design bifunctional compounds with two separate binding sites for iron and the radionuclide and to (ii)

https://doi.org/10.1021/acs.jmedchem.1c01054
J. Med. Chem. 2021, 64, 12359−12378

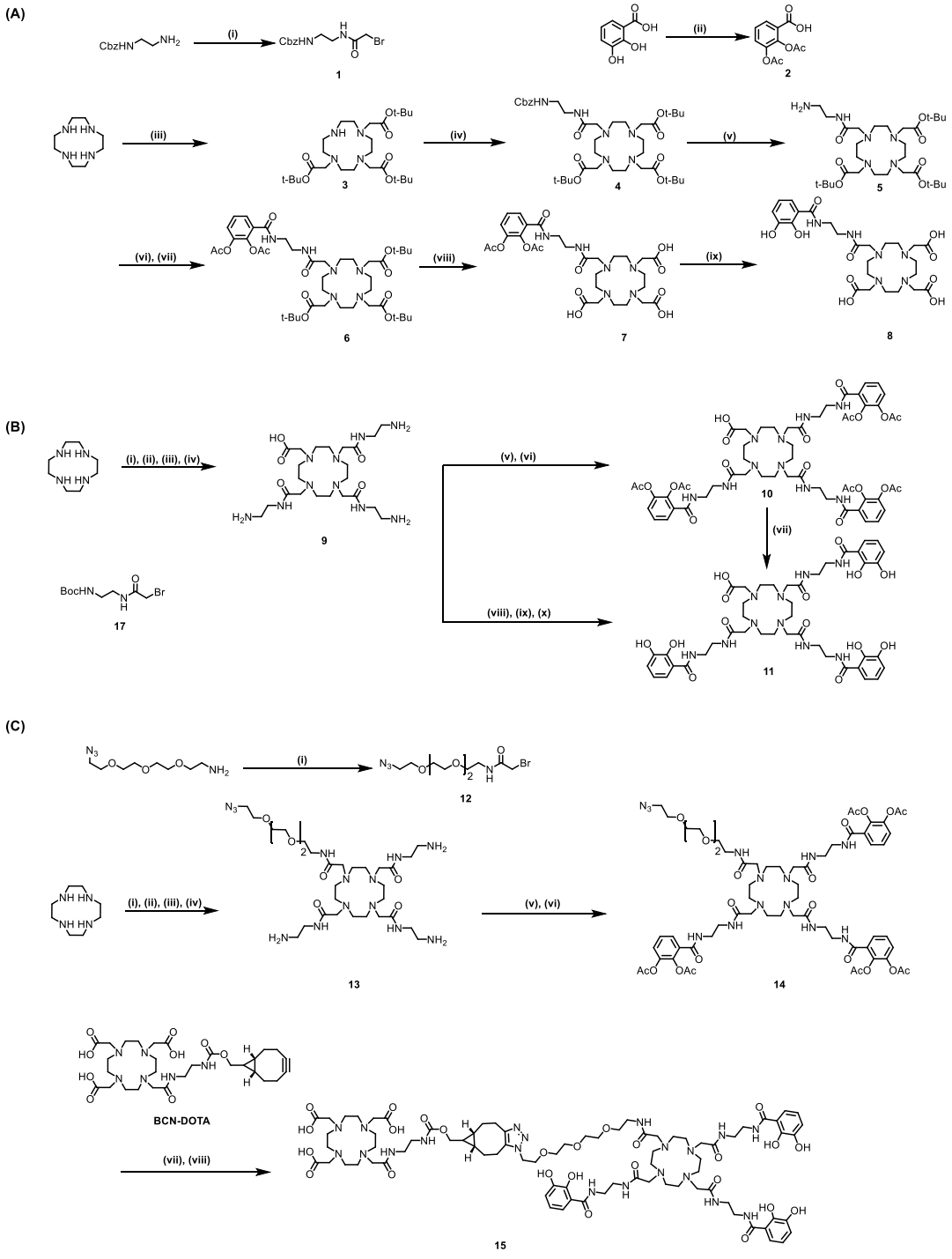

Figure 2. Synthesis of siderophore-based PET imaging agents. (A) Synthesis of precursors **7** and **8** from cyclen: (i) bromoacetyl bromide, K_2CO_3, DCM/H_2O (1:1), 3 h, 21 °C, and 87%; (ii) Ac_2O, DMAP, Et_3N, THF, 5 h, 29 °C, and 86%; (iii) ^{t}Bu 2-bromoacetate, NaOAc, DNA, 20 h, 23 °C, and quant.; (iv) **1**, K_2CO_3, MeCN, 1 h, 22 °C, and 63%, (v) 0.1 mol % Pd/C, H_2, MeOH, 1 h, 22 °C, and 92%; (vi) **2**, oxalylchloride, DCM/DMF, 1 h, and 0−22 °C; (vii) $KHCO_3$, H_2O/1,4-dioxane, 0.5 h, 23 °C, and 30%; (viii) 50% TFA, DCM/AcOH, 25 h, 23 °C (1:1), and 20%; and (ix) 20% DIPEA in MeOH, 1 h, 22 °C, and 60%. (B) Synthesis of precursors **10** and **11** from cyclen: (i) **17**, NaOAc, DMA, 20 h, and 21 °C; (ii) benzyl-2-bromo-acetate, K_2CO_3, MeCN, 22 h, and 23 °C; (iii) 25% TFA, DCM, 3 h, and 24 °C; (iv) 0.1 mol % Pd/C, H_2, MeOH, 2 h, 21 °C, and 99% within four steps; (v) **2**, oxalylchloride, DCM/DMF, 1 h, and 0−20 °C; (vi) $KHCO_3$, H_2O/1,4-dioxane, 0.5−1 h, 0−20 °C, and 35% within two steps; (vii) 20% DIPEA, MeOH, 4 h, 25 °C, and quant.; (viii) 2,3-bis(benzyloxy)benzoic acid, oxalylchloride, DCM/DMF, 1 h, and 0−20 °C; (ix) $KHCO_3$, H_2O/1,4-dioxane, 0.5−1 h, and 0−20 °C; (x) 0.1 mol % Pd/C, H_2, MeOH, 2 h, 21 °C, and 10% within three steps. (C) Synthesis of precursor **15** from cyclen: (i) bromoacetyl bromide, K_2CO_3, DCM/H_2O (1:1), 3 h, 0−25 °C, and 91%; (ii) **17**, NaOAc, DMA, 20 h, and 21 °C; (iii) **12**, K_2CO_3, MeCN, 22 h, and 23 °C; (iv) 25% TFA, DCM, 3 h, 24 °C, and quant. within four steps; (v) **2**, oxalylchloride, DCM/DMF, 1 h, and 0−20 °C; and (vi) $KHCO_3$, H_2O/1,4-dioxane, 0.5−1 h, 0−20 °C, and 39% within two steps. (vii) 20% DIPEA, MeOH, 2 h, and 25 °C; (viii) **BCN-DOTA**, MeOH/DMSO, 1× PBS, 25 °C, and 80% over two steps.

https://doi.org/10.1021/acs.jmedchem.1c01054
J. Med. Chem. 2021, 64, 12359−12378

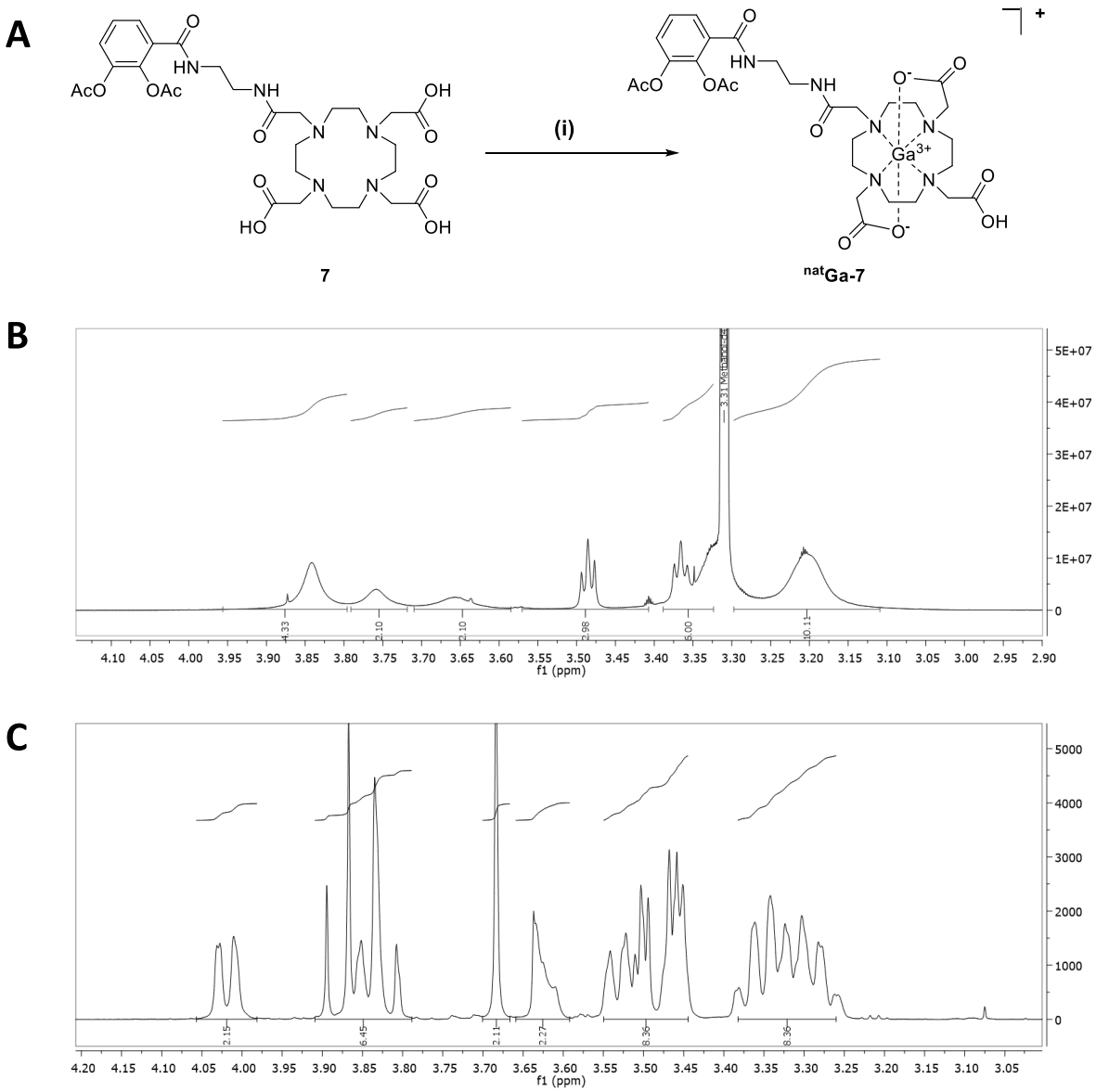

Figure 3. Formation of the "cold" Ga-complex [^{nat}Ga]7. (A) Reaction conditions: (i) $GaCl_3$, 0.5 M NaOAc buffer, pH 4.5, 95 °C, 10 min, and 84%. (B) ^{1}H NMR spectrum of **7** in the alkyl region (3.0−4.1 ppm) of the cyclen ring. (C) Characteristic reorganization of the ^{1}H NMR spectrum after of Ga^{3+} incorporation to yield complex [^{nat}Ga]7.

employ a non-natural siderophore analogue that is potentially accepted by a broad range of bacteria. This decoupling of tracer binding and uptake allows us to optimize both functions independently. In a previous study, we have qualified artificial siderophores based on the cyclen scaffold as suited to accommodate two metals, label a broad range of bacteria, and detect infections in mice using optical imaging with tagged fluorophores.[33] While our previous probes were confined to cellular and small animal imaging, the current study reports a crucial step toward translation of the probes, that is, their optimization to PET tracers for the imaging of large species including humans.

RESULTS AND DISCUSSION

Synthesis of Cyclen-Based Siderophore Analogues. We aimed to use the versatile cyclen scaffold to attach catecholate units for Fe^{3+} chelation and at the same time complex a Ga^{3+} ion via the cyclen core itself as a PET imaging tracer. In our original design,[33] cyclen was functionalized to a tetrapodal 1,4,7,10-tetraazacyclododecane-1,4,7,10-tetraacetic amide (DOTAM) to accommodate the metal for imaging.[34] However, the reaction times for Ga^{3+} incorporation were in the range of hours, which is incompatible with radiochemical synthesis and positron emitter half-life. Because the rates of metal incorporation are much higher for 1,4,7,10-tetraazacyclododecane-1,4,7,10-tetraacetic acid (DOTA)-based cores with free carboxylic acid moieties,[35] we systematically varied the number of amide-linked catechols (for Fe-complexation) versus number of carboxylates (for Ga-complexation) from 1:3 to 2:2 to 3:1 (Figure 1). In addition, the use of one DOTA and one DOTAM core that are conjugated to each other would enable a 3:3 constellation; that is, a scaffold with three gallium-68 complexing carboxylates is linked to a scaffold with three iron complexing catechol units. In order to facilitate Ga-complex formation from DOTAM moieties, α-methyl substituents, which should exert a Thorpe−Ingold effect and

https://doi.org/10.1021/acs.jmedchem.1c01054
J. Med. Chem. 2021, 64, 12359−12378

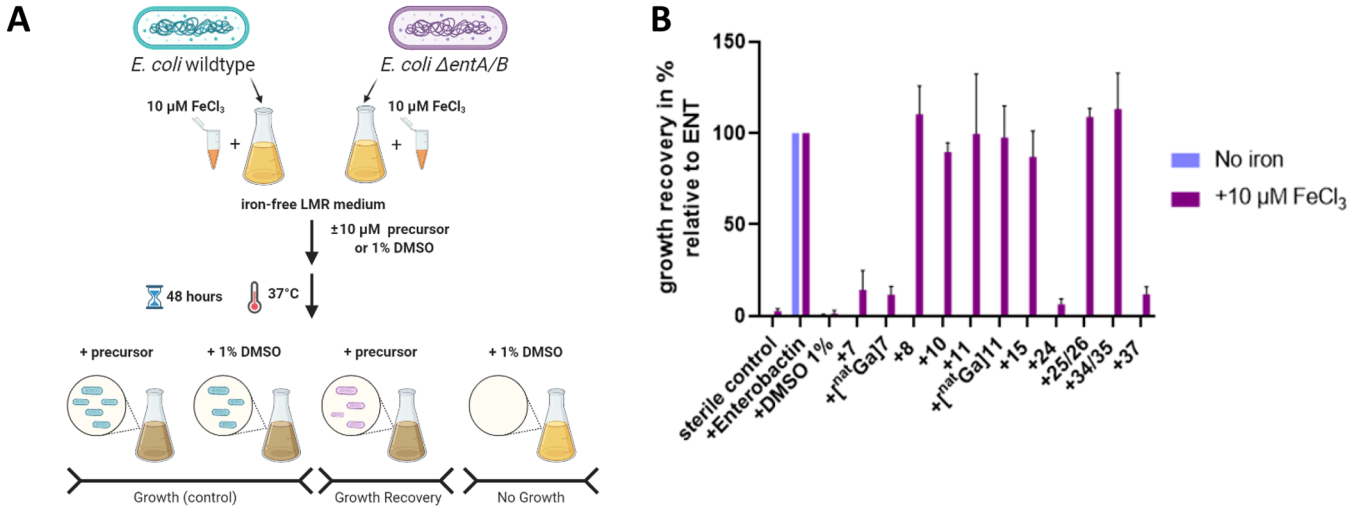

Figure 4. Growth recovery assay in the siderophore-deficient *E. coli* mutant. (A) The principle of growth recovery assay created using biorender and (B) the growth recovery in the ENT-deficient strain *E. coli* Δ*entA* in the presence of 10 μM compound ±10 μM $FeCl_3$ were assessed after incubation for 48 h at 37 °C by OD_{600nm} measurement in a plate reader. Bacteria were either grown in iron-depleted (no iron) or 10 μM $FeCl_3$-supplemented, phosphate-buffered LMR medium (n = 3). The growth relative to ENT is plotted; error bars correspond to ±standard deviation (SD).

reduce the bite angle at the cyclen core, were introduced as well.[36] The catechol units, representing bidentate iron binders, were partly masked as acetylated prodrugs, which are activated in situ in a cellular environment in order to prevent permanent inactivation of the catechol by enzymatic alkylation and to facilitate ^{68}Ga-complex formation.[37]

Starting from cyclen, we made use of optimized reaction conditions, which can yield each a specific substitution pattern from a mono- to a tri-substituted core, respectively (Figure 2). The metal-free ligands—referred to as "precursors"—were obtained by slow, sequential addition of the appropriate equivalents of alkyl bromide and base in acetonitrile with near to complete conversion and high purity. Depending on the choice of the initial substitution reaction, this strategy led to 1:3 or 3:1 catechol/carboxylate ratios. The synthesis of mono-catechol siderophore analogues started with the reaction of cyclen and *tert*-butyl bromoacetate to yield **3** (Figure 2A). The tri-substituted cyclen **3** was used as a crude product and reacted with the linker **1** under basic conditions to attach the fourth arm in 55% yield over two steps. Subsequently free amine **5** could be afforded after hydrogenolysis of the Cbz protecting group with Pd/C under a H_2 atmosphere in 92% yield. The primary amine of **5** was reacted with the in situ generated acid chloride of **2** in a two-phase Schotten–Baumann reaction to the desired amide **6** in 30% yield, which was subsequently deprotected with 50% trifluoroacetic acid (TFA)/AcOH to afford the acetylated mono-catechol **7**. The free catechol **8** was then obtained by transacetylation with 20% DIPEA in MeOH.

In order to obtain tris-catechol siderophores, cyclen was reacted first with the bromoacetamide **17** and subsequently with benzyl 2-bromoacetate under basic conditions, followed by a Boc group removal/hydrogenation sequence (Figure 2B). In this manner, intermediate **9** was obtained within four steps. The amine **9** was reacted with the freshly prepared acid chloride of **2** in a Schotten–Baumann reaction to afford the acetylated precursor **10** in 32% isolated yield within six synthetic steps. A similar sequence with **9** and the acid chloride of 2,3-bis(benzyloxy)benzoic acid, followed by hydrogenolysis, yielded precursor **11** with free catechols. This compound could also be obtained by transacetylation of **10** with 20% DIPEA in MeOH in a 31% overall yield within seven synthetic steps. The two cis- and trans-substituted di-catecholates **34** and **35** were obtained as an inseparable mixture by similar reaction sequences; the same was true for the regioisomers **25** and **26** that were alpha-methylated at the free carboxylic acids (Supporting Information, Figures S1 and S2).

The synthesis of the DOTA tris-catechol conjugate **15**, offering three carboxylates and three catechols, was commenced by reacting 2-(2-(2-(2-azidoethoxy)ethoxy)ethoxy)-ethyl-1-amine with bromoacetyl bromide to afford linker **12** (Figure 2C). Cylen and secondary bromides **17** and **12** were employed in a similar three-step sequence as shown above to afford **13**. The DOTAM **13** and the freshly prepared acid chloride of **2** yielded siderophore **14** in 36% yield within six steps. Transacetylation of **14** with 20% DIPEA in MeOH followed by strain-promoted azide–alkyne cycloaddition (SPAAC) with commercial **BCN-DOTA** yielded DOTA tris-catechol precursor **15** in 26% overall yield over nine synthetic steps.

Gallium Complexation. The ability of the cyclen-based siderophores to complex gallium ions was tested with the mono-catecholate **7**, the tris-catecholate **11**, and the DOTA tris-catechol **15**. Using a 0.5 M NaOAc buffer and $GaCl_3$, "cold" Ga-complexes could be readily prepared on a single-digit milligram scale at 95–100 °C in 10 min and yields of 18–84% (Figure 3A). The ^{1}H NMR spectra of **7**, **11**, and **15** were featured by a much better resolution in the region of 3.0–4.1 ppm upon introduction of the Ga^{3+} cation due to the metal loading into the cyclen moiety (Figures 3B, S3, and S4). According to previous studies, the metal-DOTA complex formation is a two-step process.[38] Initially, a reversible adduct (the so-called type I complex) forms. Protonation/deprotonation reactions at the carboxylic acid groups and macrocycle nitrogen protons then result in the slow conversion to a highly stable type II complex that is featured by a full coordination of the metal.[39,40] The rate of metal-DOTA complexation is higher at an elevated temperature or with more flexible macrocycles

https://doi.org/10.1021/acs.jmedchem.1c01054
J. Med. Chem. 2021, 64, 12359–12378

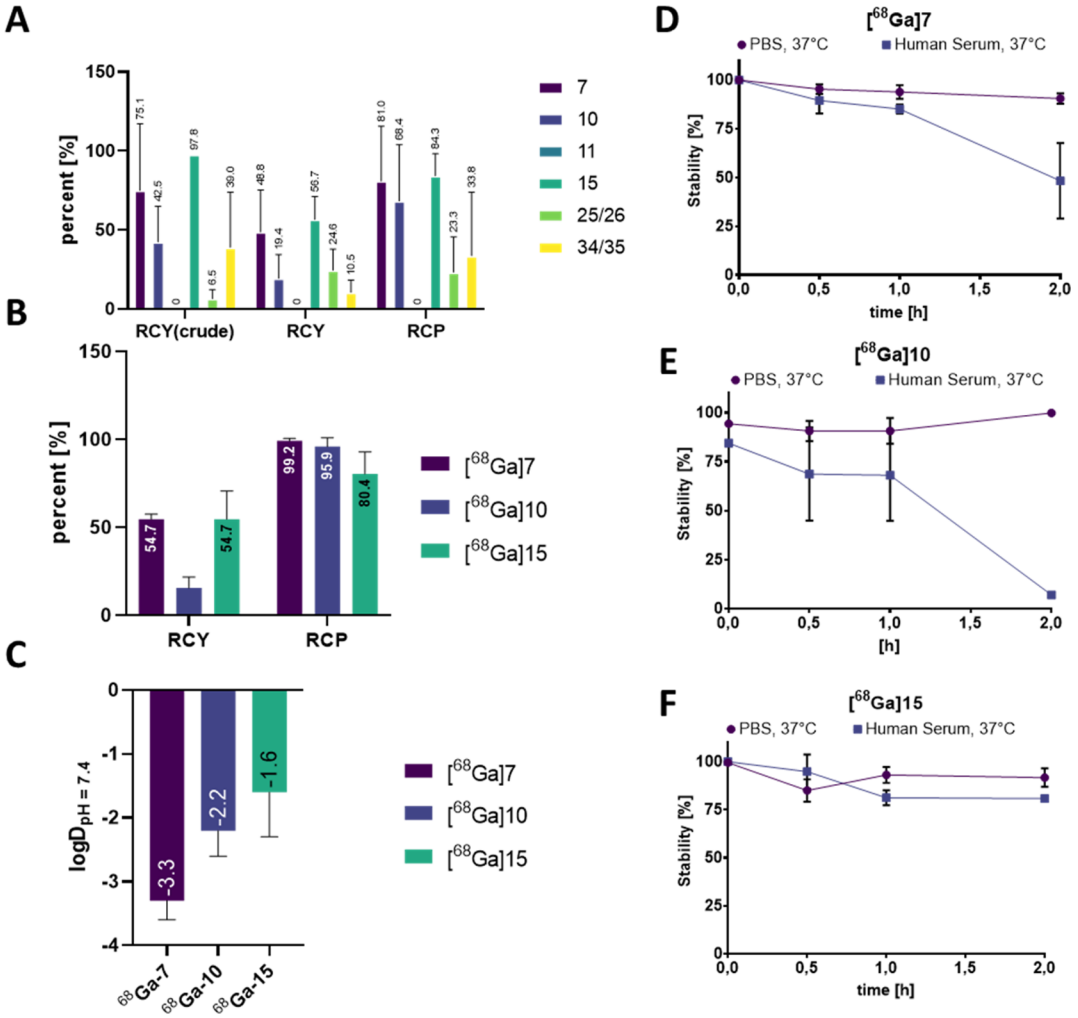

Figure 5. Radiochemical and physicochemical parameters and stability of ^{68}Ga-complexes. (A) The radiochemical yield of the crude product determined from an aliquot of the reaction solution [RCY (crude), RCY, and RCP of siderophores manually complexed with [^{68}**Ga**] are shown, min. n = 3, error bars indicate ± SD]. (B) RCP and RCY for automated radiochemical synthesis of [^{68}**Ga**]**7**, [^{68}**Ga**]**10**, and [^{68}**Ga**]**15** on an automatic synthesis module with 30 nmol precursor, min. n = 3, error bars indicate ±SD. (C) log $D_{7.4}$ values were determined in an octanol/water system, min. n = 3, error bars indicate ± SD. (D−F) Stability data of [^{68}**Ga**]**7**, [^{68}**Ga**]**10**, and [^{68}**Ga**]**15** in PBS (pH = 7.4) and human serum at 37 °C detected by radio-HPLC runs in intervals of 30 min and subsequent integration of the respective peaks, min. n = 3, error bars indicate ± SD. Acetylated and deacetylated forms are both considered.

because the exchange rate between conformational isomers increases.[35,41] Deprotonation associated with gallium complexation leads to two evident effects in the ^{1}H NMR spectra: (1) higher chemical shift values due to a deshielding effect for the methylene ^{1}Hs close in space to the central Ga cation and (2) a ^{1}H-signal split related to a fixation of the apparently fluxional DOTA unit into a rigid or semi-rigid complex. The affected protons become magnetically nonequivalent because of a defined complexation status,[39] which leads to the resolved H NMR peak pattern shown in Figures 3B, S3, and S4.

Growth Recovery Capabilities of Cyclen-Based Siderophore Analogues. Next, we tested whether the artificial siderophores were able to enter bacterial cells in free as well as in the Ga^{3+}-complexed form. For this purpose, a surrogate assay that measured the compound-mediated delivery of iron into bacteria based on growth recovery was applied (Figure 4A).[33] The Δ*entA* and Δ*entB* mutants of *E. coli* BW25113, which cannot biosynthesize their endogenous siderophore enterobactin (ENT), were unable to grow under iron-depleted conditions as well as under Fe^{3+}-supplemented conditions [Figures 4B and S5A, dimethyl sulfoxide (DMSO) control]. Because these strains are reliant on exogenous siderophores to grow under iron-limited conditions, the exogenous addition of the natural siderophore ENT (10 μM) restored the growth of the *E. coli* Δ*entA* and Δ*entB* mutants. Remarkably, also the supplementation of DOTAM-based siderophore analogues (10 μM) fully rescued the growth in 7 out of 11 cases for both mutant strains. The most efficient growth recovery was observed for the DOTA tris-catechol **15**, as well as the tris-catechol **10** and **11**. Also, the di-catechols **25**/**26** and **34**/**35** were able to relieve iron deficiency. In contrast, the mono-catechols were generally less potent. Interestingly, [^{nat}**Ga**]**11** was also accepted as a siderophore and exhibited a potency that was comparable to the uncomplexed analogue **11**. A less pronounced but still measurable growth recovery can also be found for the mono-catechols **7** and [^{69}**Ga**]**7**. The deacetylated mono-catechol **8** was found to be more efficient than **7** in the *E. coli* Δ*entA* mutant. The effect of α-methyl substituents can be assessed by comparing the methylated mono-catechol **8** with its unmethylated congener **24**. Likewise, the methylated

https://doi.org/10.1021/acs.jmedchem.1c01054
J. Med. Chem. 2021, 64, 12359−12378

tris-catechol **37** can be compared to the unmethylated **10**. In both cases, the methyl-substitution led to an impairment of growth recovery, indicating a decreased uptake of the complexes. In sum, these results demonstrate that the cyclen-based probes can shuttle Fe^{3+} into the bacterial cell, indicating their internalization, even when they are loaded with a Ga^{3+} cation.

The growth recovery data from the pyochelin and pyoverdine-deficient *P. aeruginosa strain* Δ*pvdD* Δ*pchE-F* showed that the exogenous addition of DOTAM-based siderophore analogues could relieve iron deficiency to an extent that was comparable to that of the natural siderophore pyoverdine (Figure S5B). A significant increase in efficiency compared to its result in the *E. coli* mutants was observed for compound **7**. Compounds **8**, **10**, and **15** were found to exhibit retained activity in the *P. aeruginosa* mutant. The similar efficiency across two bacterial species is encouraging for the applicability of our probes.

With a readout after 48 h, the growth recovery assay mimics the long-term iron supply into bacteria. An in vivo PET scan with a gallium-68 ($t_{1/2}$ = 67.71 min[42]) complexed tracer takes about 60 min and is rather short in comparison. In vitro uptake experiments during similar timeframes with radiolabeled siderophore analogues would resemble the in vivo setup more closely, and an estimation of the maximum and minimum tracer uptake could be gained by comparing wild-type and siderophore-deficient strains. Those studies will be important for a future candidate selection.

According to the literature, the release mechanism of ferric iron from siderophores is siderophore and species dependent.[43] The release can occur in the periplasm or cytoplasm, and it is mediated either by intracellular Fe-siderophore reductases or by Fe-siderophore hydrolases.[44,45] For example, the tris-catechol siderophore ENT is degraded via a lactone cleavage by esterases such as Fes or IroD in the cytoplasm, followed by the reduction of Fe(III) to Fe(II).[46] The mechanism for artificial DOTAM siderophores is unknown. Given that they lack a hydrolysable backbone, we assume that the release is mediated either by metal reduction or by the metabolism of the catechol units. The mono- and di-catechol siderophores with a weaker binding affinities and redox potentials are easily amenable to ligand exchanges as well as reductions.

Chemical Stability and Cytotoxicity. The chemical stability of the Ga^{3+}-free precursors **7**, **8**, **24**, **11**, **37**, and **34**/**35** was measured in phosphate-buffered saline (PBS) at 37 °C over a period from 24 to 96 h by liquid chromatography (LC)/ultraviolet (UV)/mass spectrometry (MS) (see Figure S6). All compounds showed a stability of at least 60% over 4 h under the given conditions, which are deemed as sufficient for PET measurements (Figure S6A). For prodrugs, the acetyl group stability gradually declined, and no acetylated compound could be detected after 24 h (Figure S6B), which is in accordance with previously published data.[33] The cellular cytotoxicity of Ga^{3+}-free precursors **7**, **8**, **11**, **15**, **24**, **25**/**26**, **34**/**35**, and **37** as well as Ga^{3+}-complexed siderophores [^{nat}**Ga**]**7** and [^{nat}**Ga**]**10** was tested in the five eukaryotic cell lines L929, A549, KB-3-1, MCF-7, and FS4-LTM. All compounds were classified as noncytotoxic up to concentrations of 100 μM (Table S1).

Radiochemical Synthesis. Representative mono-, di-, and tris-catecholates (**7**, **25**/**26**, **34**/**35**, **10**, **11**, and **15**) that induced growth recovery, exhibited good stability in PBS, and showed no cytotoxic effects were selected for radiochemical labeling with gallium-68. For manual labeling, 30−50 nmol precursor was mixed with unprocessed gallium-68 chloride. The complexation process was assessed by (i) radiochemical yield of the crude product determined from an aliquot of the reaction solution by high-performance liquid chromatography (HPLC) [radiochemical yield (RCY) (crude)], (ii) the RCY of the purified tracer, defined as the amount of activity (decay corrected) in the product expressed as the percentage (%) of the related starting activity, and (iii) the radiochemical purity (RCP), defined as the proportion of the total radioactivity in the sample which is present as the desired radiolabeled species.[47] The precursor **15** reached the highest values for RCY (crude) (97.8%), RCP (84.3%), and RCY (56.7%), followed by the mono-catechol **7** and the tris-catechol **10** (Figure 5A). Interestingly, **11** demonstrated dramatically decreased RCY (crude) and RCP compared to the acetylated prodrug **10**. Likewise, the complexation of **8** with "cold" gallium ions was less efficient than that of **7** (data not shown). Stable complexes with ENT mimics such as TREN-CAM (tripodal ENT analogue-catecholate coordinating moieties), which resisted transchelation even with 1000-fold excess of desferrioxamine, provide evidence for the gallium-68 complexing ability of catechols.[48] In contrast to these compounds, our siderophore analogues exhibit two chelation centers—at the catechol units and at the cyclen moiety. Therefore, we introduced transient masking groups (acetyl) at the catechols to facilitate the rapid formation of stable gallium-68 complexes at the cyclen unit. The significantly higher RCY for [^{68}**Ga**]**10** compared to the deacetylated tracer [^{68}**Ga**]**11** supports this assumption. Because a fast complexation is imperative due to the short half-life of gallium-68, the precursor **11** was deselected. In contrast, **15** with a spatially separated DOTA moiety achieved high RCY (crude), RCP, and RCY without acetylated groups. The di-catecholates **25**/**26** and **34**/**35** had rather low RCPs and RCYs. Because **25**/**26** and **34**/**35** had the additional drawback of being regioisomeric mixtures, the di-catecholates were no longer pursued. Thus, we conclude that the spatial separation of an optimal ^{68}Ga-chelator (DOTA) from the iron-chelating DOTAM siderophore facilitates the formation of stable ^{68}Ga-complexes. Based on the radiochemical data, the three siderophores **7**, **10**, and **15** were selected for further studies.

The radiochemical synthesis of [^{68}**Ga**]**7**, [^{68}**Ga**]**10**, and [^{68}**Ga**]**15** was first optimized manually regarding the EtOH content, heating time, pH value, and purification cartridges (Table S2 in the Supporting Information). Based on the manual procedure, the precursors were complexed on an automated synthesis module to minimize radioactive exposure and standardize the complexation conditions and the corresponding RCP/RCY for in vivo studies (Figure 5B). **7** (30 nmol) could be labeled within 8 min and purified via a ^{t}C18 light cartridge, while precursor **15** was labeled within 6 min and purified via a HLB light cartridge. Precursor **10** needed 25 min of synthesis time. The longer time might be attributed to the presence of only one free carboxylate in the cyclen and increased sterical hindrance by the side groups. The highest RCYs were afforded by [^{68}**Ga**]**15** and [^{68}**Ga**]**7**, while [^{68}**Ga**]**7** reached the highest purity. The molar activity ranged between 2.6 and 18.3 GBq/μmol (70.3−495.8 mCi/μmol) for [^{68}**Ga**]**15**, 2.9−7.6 GBq/μmol (78.2−206.3 mCi/μmol) for [^{68}**Ga**]**7**, and 0.6−1.4 GBq/μmol (16.7−38.7 mCi/μmol) for [^{68}**Ga**]**10**. The lipophilicity of all the three ^{68}Ga-complexed tracers was determined in an octanol/water matrix, with [^{68}**Ga**]**7** being the most hydrophilic (log D = −3.3) and

https://doi.org/10.1021/acs.jmedchem.1c01054
J. Med. Chem. 2021, 64, 12359−12378

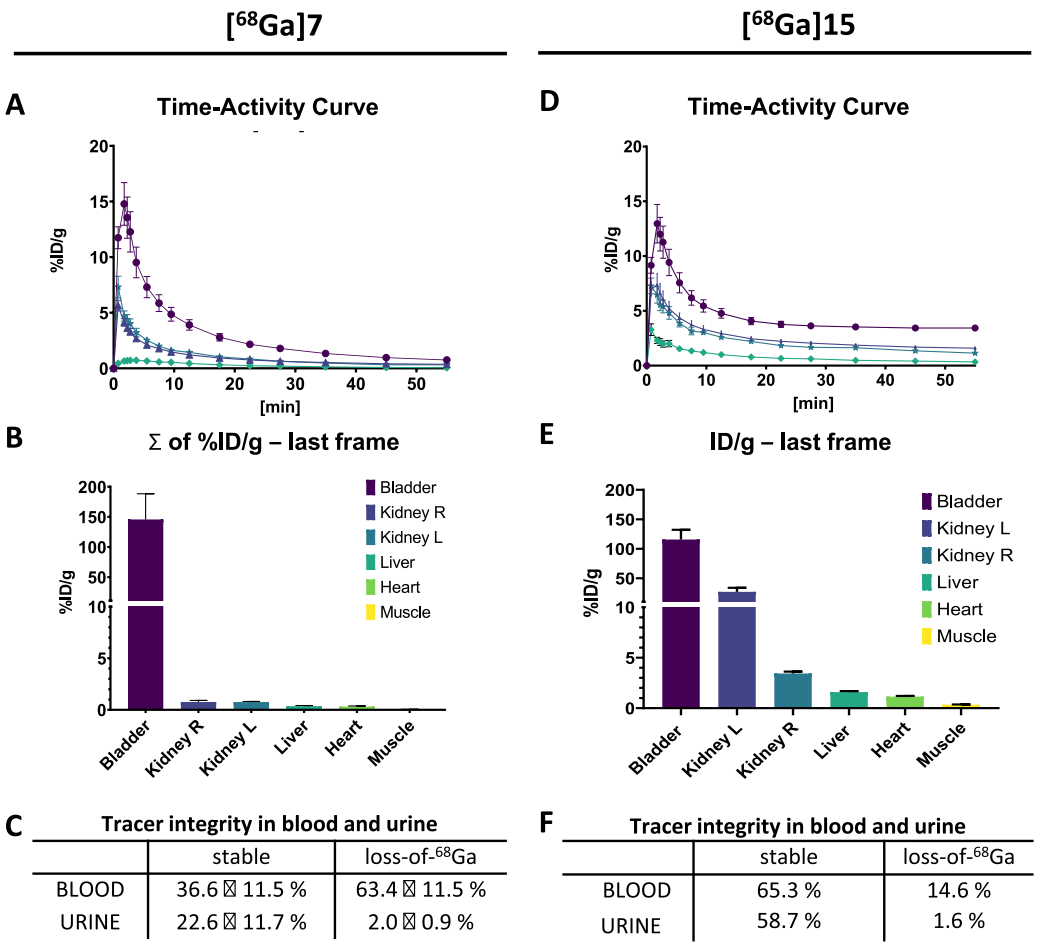

C	stable	loss-of-^{68}Ga
BLOOD	36.6 ± 11.5 %	63.4 ± 11.5 %
URINE	22.6 ± 11.7 %	2.0 ± 0.9 %

F	stable	loss-of-^{68}Ga
BLOOD	65.3 %	14.6 %
URINE	58.7 %	1.6 %

Figure 6. Biodistribution of [^{68}Ga]**7** [left side, (A−C)] and [^{68}Ga]**15** [right side, (D−E)] in male C57Bl/6N mice over 60 min of dynamic PET imaging. (A + D) Representative time activity curves (TAC) display the biodistribution of [^{68}Ga]**7** or [^{68}Ga]**15** tracers for six organs (left and right kidney, bladder, liver, heart, and muscle) in the course of 1 h of dynamic PET/CT imaging (n = 6, error bars indicate ± SD). Detailed graphs showing all 32 frames can be found in Figures S9 and S10. In (B + E), the % injected dose/organ weight during the last time frame (50−60 min) of dynamic PET/CT scan (% ID/g), is plotted, n = 6, error bars indicate ± SD. (C + F) Tracer integrity and formation of hydrophilic metabolites in blood and urine samples (each n = 6, error calculated as ± SD) after 60 min of dynamic PET/CT scan determined by radio-HPLC measurements.

[^{68}Ga]**15** notably more lipophilic (log D = −1,6, Figure 5C). The stability of the radiotracers in PBS and in human serum at 37 °C was evaluated by radio chromatograms directly after synthesis for 2 h (Figures 5D−F and S7). As found for the uncomplexed precursors, all the three compounds were >80% stable in PBS for 2 h. However, [^{68}Ga]**7** and [^{68}Ga]**10** displayed some instability in the serum: For [^{68}Ga]**7**, 19.1 ± 6.2% gallium-68 were released after 2 h of incubation. Moreover, the tracer deacetylated, resulting in 58.9 ± 22.0% deacetylated [^{68}Ga]**7** within 2 h. [^{68}Ga]**10** (91.4 ± 1.8%) was deacetylated in the serum after 2 h. Stepwise enzymatic deacetylation in human serum, and hence release of the free catechol moieties of both complexes over the course of 2 h, was accompanied by a shift to smaller (more polar) retention times (see Figure S7A,C, right), corresponding to the conversion of the prodrug to the active drug. As [^{68}Ga]**15** did not bear any acetyl groups, deacetylated metabolites were not observed, but a more lipophilic metabolite was formed after 2 h (see Figure S7B). Still, 80.8 ± 0.8% [^{68}Ga]**15** remained stable for more than 2 h in the serum.

While [^{68}Ga]**15** displayed high RCY and tracer stability compared to other bacteria-specific PET tracers,[12,18,25,27,29,30] [^{68}Ga]**7** could be further improved by either installing a fourth carboxylate donor group or instead a smaller NOTA chelator to form more stable gallium-68 complexes.[49] Free catechol-assisted trans-chelation or hydrolysis was successfully masked by the introduction of transient protection groups. Deacetylation of the catechol moieties occurred over ca. 6 h in PBS (pH 7.4), as shown in Figure S6B and in a previous study.[33,50] However, the stability and radio HPLC data of [^{68}Ga]**7** (Figures 5 and S7) suggest a more rapid reaction to the free catechol in blood than in PBS. Therefore, alternative masking groups with higher stability, for example, sialylethers or acetals, could be evaluated with respect to species-specific higher hydrolase activities.[51]

Biodistribution Studies in Mice. The biodistribution properties of [^{68}Ga]**7**, [^{68}Ga]**10**, and [^{68}Ga]**15** were tested in healthy, male C57BL/6N mice (n = 6 per tracer). For this purpose, 12.8 ± 2 MBq (0.35 ± 0.05 mCi) [^{68}Ga]**7**, 10.8 ± 1.6 MBq (0.3 ± 0.04 mCi) [^{68}Ga]**15**, or 10.7 ± 1.5 MBq (0.29 ± 0.04 mCi) [^{68}Ga]**10** were administered via a catheter in the lateral tail vein [intravenous (iv) injection]. The tracer accumulation was monitored over 60 min by dynamic PET/Computed Tomography (CT) scans in 32 frames. [^{68}Ga]**7** exhibited almost exclusively renal clearance with low blood pool retention and fast clearance from examined organs (Figure 6A). In the last frame, unspecific tracer uptake in the healthy muscle tissue was negligible (0.05 ± 0.01% ID/g,

https://doi.org/10.1021/acs.jmedchem.1c01054
J. Med. Chem. 2021, 64, 12359−12378

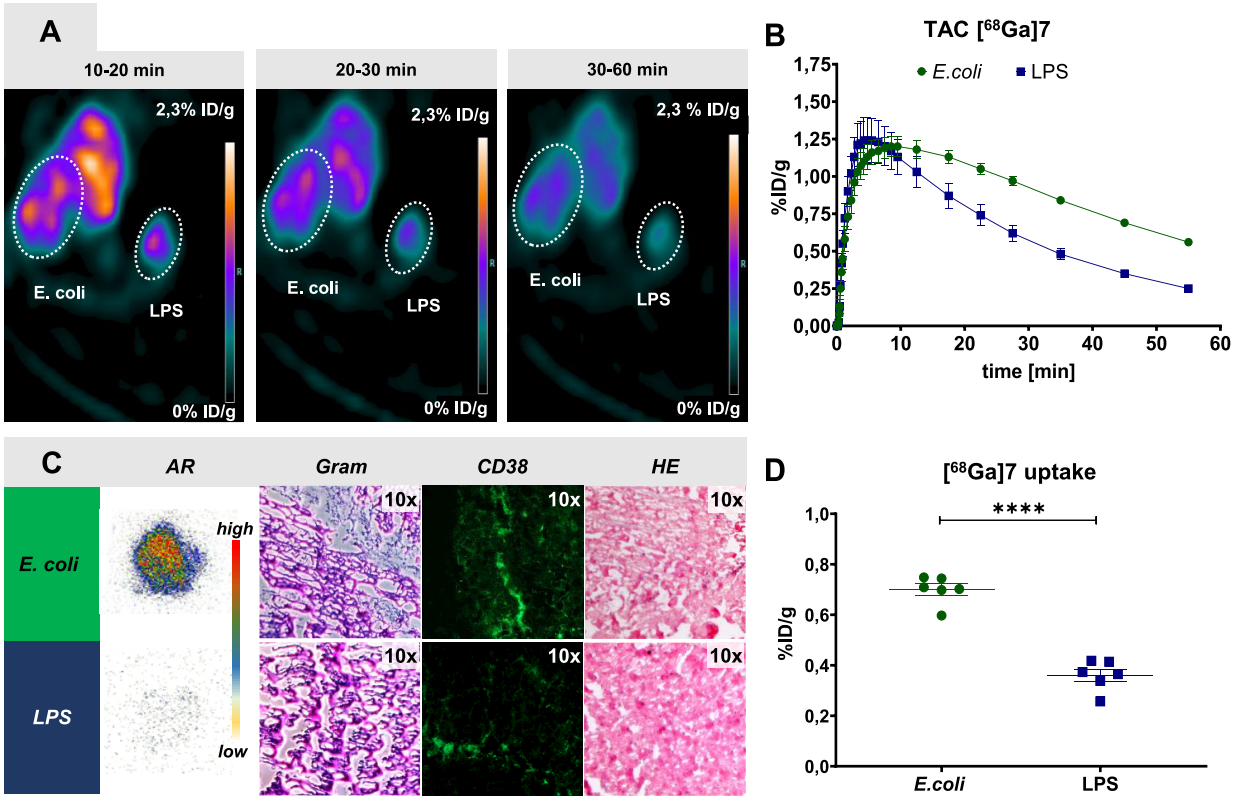

Figure 7. In vivo PET imaging in mice infected with *E. coli* with [^{68}Ga]7. (A) 3.0 × 10^7 CFUs *E. coli* (ATCC47076) was administered *i.m.* into the left leg, and 27 μg of LPS was administered *i.m.* into the right leg 24 h before imaging (n = 6 animals, male C57Bl/6N mice). [^{68}**Ga**]**7** was prepared directly prior to the imaging experiment and injected iv into the tail vein. Dynamic PET scans were performed for 60 min using a micro PET/CT (transaxial view displayed, further data, and video compilation are given in the Supporting Information). (B) TAC of decay-corrected [^{68}**Ga**]**7**, error bars are ±SD. (C) Dissected *M. gastrocnemius* after 60 min of PET/CT scan were imaged by autoradiography (AR), underwent Gram staining for bacteria (blue areas), immune histology with an anti-CD38 antibody (CD38) for macrophages (green fluorescence), and hematoxylin and eosin stain for cells and tissue. The upper row shows the images of the *E. coli*-infected left muscle, while the lower row shows the images of the LPS-injected right muscle. (D) The accumulated dose % ID/g of [^{68}**Ga**]**7** over the course of the last 30 min of dynamic PET/CT scans was 1.9-fold higher in *E. coli*-infected compared to LPS-injected muscles (****: p-value <0.0001).

Figure 6B). [^{68}**Ga**]**15** showed a similar kinetic compared to [^{68}**Ga**]**7**, that is, a rapid, mainly renal clearance and a low blood pool retention, but exhibited a higher liver accumulation (Figure 6D), correlating well with its higher lipophilicity. The uptake into healthy muscle amounted to 0.34 ± 0.05% ID/g (Figure 6E). [^{68}**Ga**]**10** was excreted via the kidneys and liver but showed a higher background activity in blood, with longer average retention periods in the respective imaged organs (Figure S8). The nonspecific uptake of [^{68}**Ga**]**10** in healthy muscle during the last 10 min of imaging amounted to 0.5 ± 0.09% ID/g.

Only 36.6 ± 11.5% of [^{68}**Ga**]**7** could be detected in blood after 1 h of imaging, as 63.4% ± 11.5% hydrophilic metabolites were formed instead. In urine, the tracer was mainly detected in its deacetylated, active form (ca. 75.4%), with a highly hydrophilic metabolite amounting to 2.0 ± 0.9% and the acetylated intact [^{68}**Ga**]**7** to 22.6 ± 11.7% (Figure 6C). Stable [^{68}**Ga**]**15** was detected in blood as well as in urine, while the formation of metabolites was higher in blood (14.6%) than in urine (1.6%). Only 1.3 ± 1.5% acetylated and mostly deacetylated (95.4 ± 3.5%) [^{68}**Ga**]**10** could be detected in blood. The tracer was detected in urine in a relative quantity of 42.1% ± 35.1%, accompanied by formation of metabolites that accounted for 29.8 ± 25.1% (Figure S8). Moreover, [^{68}**Ga**]**10** seems to exhibit a loss of gallium-68, since an increased liver uptake and the highest unspecific uptake in healthy muscle were observed, which indicate transmetalation with transferrin in blood.[52] Based on the poor radiochemical yield and unspecific blood pool retention, [^{68}**Ga**]**10** was not considered for the subsequent infection model.

PET/CT Imaging of *E. Coli* Infected Muscle versus Sterile Inflamed Muscle in Mice. The best suited tracers [^{68}**Ga**]**7** and [^{68}**Ga**]**15** were tested in an in vivo infection model. In order to evaluate whether the tracers could differentiate between a bacterial infection and a sterile inflammation, 3 × 10^7 CFU of *E. coli* were injected into the *Musculus gastrocnemius* of the left leg, and 27 μg of lipopolysaccharide (LPS) was injected into the right leg in male C57BL/6N mice. LPS induced a sterile inflammatory reaction, which should not be detectable by tracers that specifically visualize bacteria. Twenty hours after this challenge, 11.6 ± 0.8 MBq (0.31 ± 0.02 mCi) [^{68}**Ga**]**15** (n = 8) or 11.8 ± 1.5 MBq (0.32 ± 0.04 mCi) [^{68}**Ga**]**7** (n = 6) were injected iv, respectively, and dynamic PET scans were acquired.

[^{68}**Ga**]**7** showed a rapid clearance in the infection setting, as already observed in an uninfected mice. A higher uptake of the tracer into the substantially enlarged infected muscle compared to the inflamed muscle was evident by visual inspection of the PET scan (Figure 7A and Supporting Information Video S1). The tracer accumulated rapidly in both legs within the first 10 min, but the subsequent decrease was faster in the sterile inflamed muscle (Figure 7B).

https://doi.org/10.1021/acs.jmedchem.1c01054
J. Med. Chem. 2021, 64, 12359−12378

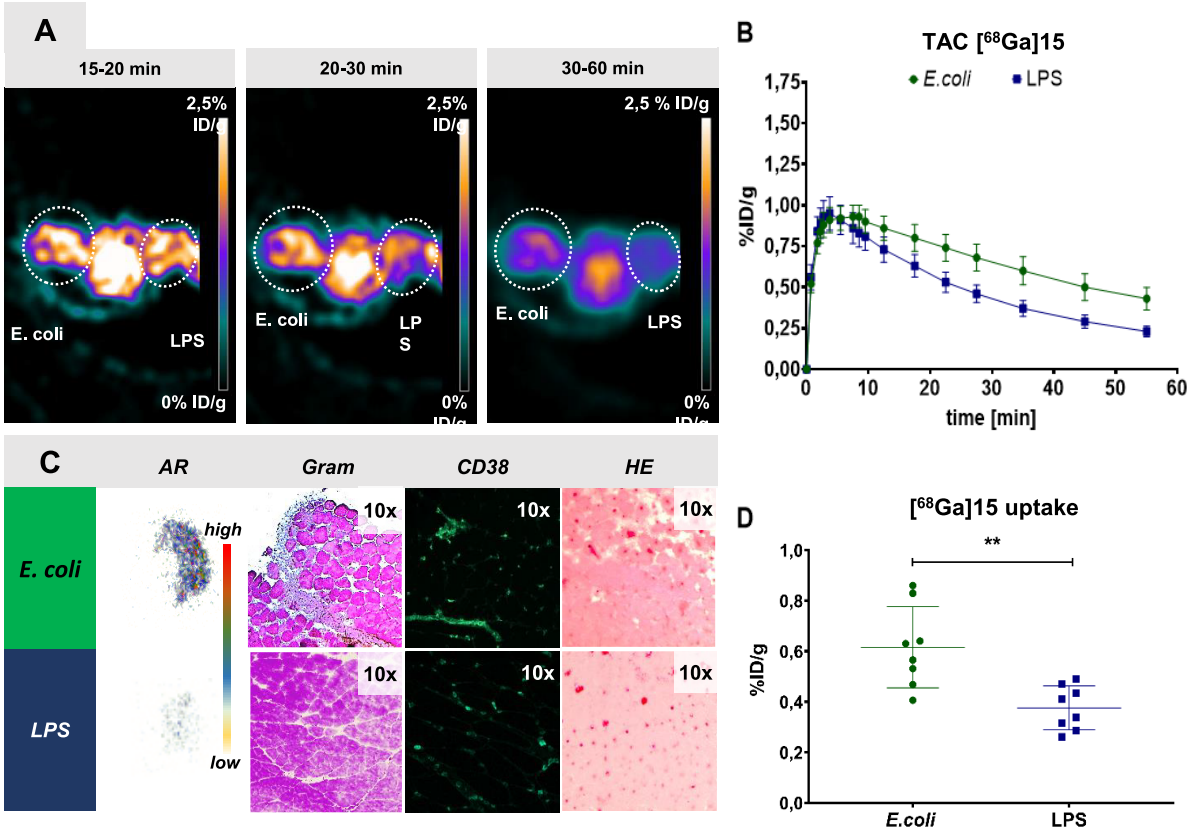

Figure 8. In vivo PET imaging in mice infected with *E. coli* with [^{68}Ga]15. (A) 2.2 × 10^7 CFU *E. coli* were administered *i.m.* into the left leg and 27 μg LPS was administered *i.m.* into the right leg 24 h before imaging (n = 8 animals, male C57Bl/6N mice). [^{68}Ga]**15** was prepared directly prior to the imaging experiment and injected iv into the tail vein. Dynamic PET scans were performed for 60 min using a micro-PET/CT (transaxial view displayed, further data, and video compilation are given in the Supporting Information). (B) TAC of decay-corrected [^{68}Ga]**15**, error bars are ± SD. (C) Dissected *M. gastrocnemius* after 60 min of PET/CT scan were imaged by autoradiography, underwent Gram staining for bacteria (blue areas), immune histology with an anti-CD38 antibody (CD38) for macrophages (green fluorescence), and hematoxylin and eosin stain for cells and tissue. The upper row shows images of the *E. coli* infected left muscle, while the lower row shows images of the LPS-injected right muscle. (D) The accumulated dose % ID/g of [^{68}Ga]**15** over the course of the last 30 min of dynamic PET/CT scans was 1.7-fold higher in *E. coli* infected compared to LPS-injected muscles (**: p-value <0.0035).

Semi-quantitative analysis, based on the sum of regions of interest of the last half hour of dynamic PET scan, showed an increased uptake of [^{68}Ga]**7** into the infected muscle of 0.67 ± 0.05% ID/g in comparison to the sterile inflamed muscle (0.36 ± 0.06% ID/g uptake, p < 0.0001; Figure 7D). The accumulated dose % ID/g is 11-fold higher in the infected muscle than in the healthy muscle (see Figure 6). This indicates that [^{68}Ga]**7**, despite its structural simplicity, can distinguish between bacterial infections, sterile inflammation, and healthy tissue in vivo. The autoradiographic examination of the dissected muscles confirmed the PET scan results, as an increased uptake of the tracer into the infected versus the inflamed muscle was clearly visible (Figure 7C). Furthermore, Gram staining of the dissected muscles confirmed the presence of bacteria in the infected muscle, whereas expectedly, no bacteria were detected in the sterile LPS inflammation. On the contrary, immune staining with an anti-CD38 antibody identified invasion of macrophages in both muscles (Figure 7C).

For the DOTA tris-catechol [^{68}Ga]**15**, tracer clearance in *E. coli*/LPS-challenged mice was as rapid as in noninfected animals. Similar to [^{68}Ga]**7**, an increased uptake into the infected muscle was visible 15 min after injection (Figure 8 and Supporting Information Video S2). A semi-quantitative analysis of the last frame revealed that the uptake into the *E. coli*-infected muscle amounted to 0.51 ± 0.18% ID/g, 1.7-fold higher than into the sterile inflamed muscle (0.30 ± 0.09% ID/g; p = 0.035; Figure 8D). The autoradiographic imaging of the dissected muscle also confirmed a higher uptake of [^{68}Ga]**15** into the *E. coli* infected muscle (Figure 8C). In comparison to [^{68}Ga]**7**, a lower %ID/g over time could be accumulated, but a differentiation between infected and sterile inflamed muscle was possible. Autoradiographic images of the dissected muscles confirmed the PET/CT results and even showed a stronger difference between the infected muscle and the muscle with sterile LPS inflammation. Gram staining confirmed the presence of bacteria in the infected muscle, while no bacteria were detected in the sterile LPS inflammation. Expectedly, immune staining with an anti-CD38 antibody identified invasion of macrophages in both muscles.

The CD38-positive stains (Figures 7 and 8) figuratively depict the common response of the immune system (macrophage infiltration) to *E. coli* infection and sterile inflammation. In general, the bioavailability of free iron lies in the order of ~10^{-18} M, that is, very low. Upon LPS-induced sterile inflammation, an iron anemic environment is observed at the injection site, with low Hb, even lower iron content in Hb and elevated levels of hepcidin.[53] An enrichment of siderophore

https://doi.org/10.1021/acs.jmedchem.1c01054
J. Med. Chem. 2021, 64, 12359−12378

analogues at the inflammation site in the absence of bacteria would have to occur through unspecific host or immune cell uptake, but this was not indicated in the biodistribution studies (Figure 6). Moreover, the TonB-dependent siderophore uptake machinery is unique to prokaryotes, and active internalization by bacterial siderophore receptors occurs faster than unspecific uptake by host cells. Thus, the hypoferremia of nonsterile inflammation as well as the probe uptake mechanism all constitute advantages that contribute to the specificity of siderophore-based bacterial imaging probes.

An important point concerns the pathogen specificity and selectivity of the probes. Prokaryotes are able to hijack iron-bound siderophores synthetized by other pathogens as the so-called "xenosiderophores". An invading microbe expresses a manifold of heterologous and homologous, chelator-specific siderophore outer membrane receptors (OMRs) for the acquisition of iron from the most readily attainable source.[54] However, PET imaging with natural siderophores such as pyoverdine produced by *P. aeruginosa* was highly specific for this bacterial species and showed no accumulation in others.[29] The uptake of a gallium-68-labeled DFO-B tracer via hydroxamate OMRs (e.g., *FpvA*) into *P. aeruginosa* and *Staphylococcus aureus* was successful as expected but marginal in *E. coli* strains lacking the DFO-B transport machinery.[30] The siderophore analogues described herein target catechol-specific OMRs known to be expressed in *P. aeruginosa* (*PfeA*),[55] *E. coli,* and *Klebsiella pneumoniae* (*FepA*).[56,57] Further studies indicate that other pathogens such as *S. aureus*, *Salmonella typhimurium* and *Yersinia enterocolitica* are also able to seize catechol-based xenosiderophores such as ENT for their iron supply.[58] The catecholate-based siderophores anchored on an artificial DOTAM scaffold was shown to label to a broad range of pathogens before.[33] This demonstrates its function as a xenosiderophore, and we hypothesize that simple artificial scaffolds may find broader acceptance compared to distinct natural siderophores such as pyoverdine. However, the specificity of the current probes [^{68}Ga]**15** and [^{68}Ga]**7** and also the variance among the isolates of a given species including defined, catecholate receptor-deficient strains, requires an experimental determination in future studies.

While the cyclen scaffold allows the versatile attachment of siderophore groups as well as additional effectors, it has disadvantages concerning tracer accommodation compared to NOTA-based chelators. First, DOTA-based chelators are considered too wide and thus reduce the thermodynamic stability of the formed complex, whereas NOTA chelators offer a better match for the small Ga^{3+} ion reflected in the 10-fold higher thermodynamic stability constant than DOTA.[59−61] Due to the reduced complex stability, cyclen scaffolds run the risk of transmetalation leading to decreased RCY. Second, DOTA chelators exhibit slower complexation kinetics and accordingly require a higher temperature and elongated reaction times compared to NOTA complexes.[62] In line with this, we could observe that more substitutes on the cyclen scaffold lead to a slower complex formation, reflected in the gained radiochemical yield and the elongated reaction time. Thus, an expansion of the concept to NOTA chelators might lead to further improved probes.

CONCLUSIONS

We have expanded the suite of applications for artificial, cyclen-based siderophores to PET imaging in order to enable the monitoring of infections in large animals. The compounds were synthetized via robust and scalable synthetic pathways in up to eight steps in a modular manner and discriminated through a suite of chemical and biological assays (Figure S11). Notably, the compounds could simultaneously host a $^{68}Ga^{3+}$ for PET imaging in their cyclen core and still serve as efficient xenosiderophores in *E. coli*. A reduced number of catechols clearly led to lower growth recovery. However, two and even one catechol are capable of a growth recovery; this finding is in line with the fact that many siderophore−antibiotic conjugates employ a single bidentate iron-binding moiety to enhance their uptake.[31] The α-methyl variants did neither improve bacterial growth recovery nor radiochemical labeling and therefore seems redundant in the scaffolds investigated here. For six selected precursors, manual and automated radiochemical synthesis procedures were established successfully to yield the respective ^{68}Ga-complexed PET tracers. Two bacteria-targeted PET tracers, [^{68}Ga]**7** and [^{68}Ga]**15**, displayed favorable biodistribution and stability properties and could reliably distinguish *E. coli* infections from LPS-induced, sterile inflammation in mice. While active bacterial uptake should be superior in the DOTA tris-catechol [^{68}Ga]**15**, the ease of synthesis but also the imaging data speak for [^{68}Ga]**7**. These compounds expand the yet limited arsenal of molecular probes for bacterial imaging in large animals. In particular, we found that addressing the bacterial iron uptake system with non-natural, structurally rather simple siderophores is a viable and efficient strategy to visualize infections in vivo. Compared to previous siderophore-PET probes, the separation of iron and PET-tracer binding sites allows us to also accommodate other metal cations (e.g., ^{111}In or ^{64}Cu) that might fit less well into the siderophore binding site that was optimized for iron. The versatile scaffold, well-amenable to further modifications,[34,63] allows us to fine-tune properties and/or to introduce additional functionalities such as an antibiotically active moiety to obtain full bacteria-targeted theranostics. Indeed, a structural optimization is indicated to further improve parameters such as tracer stability in vivo or enrichment in bacteria. The findings also pave the way for siderophore-based PET imaging in larger, nonrodent species.

EXPERIMENTAL SECTION

Chemical Synthesis. Chemical and reagents were purchased from commercial vendors (TCI, Carl Roth, Baker and Sigma-Aldrich), if not stated otherwise, and employed without further purification in the below synthetic procedures. For synthesis, solvents with purity grade 99.5%, extra dry, absolute, AcroSeal, Acros Organics were used. Work up procedures and purifications solvents were either HPLC or p. A. grade. Glassware was oven-dried prior to synthesis. Reaction progress was controlled by thin layer chromatography (TLC) or LC-coupled MS (LCMS). All compounds had purity ≥95% as determined by high-performance LC (UV detection) and ^{1}H-/^{13}C NMR analysis.

Benzyl(2-(2-bromoacetamido)ethyl)carbamate (1). According to a literature procedure from Ferreira, to a white suspension of *N*-Cbz-ethylendiamine (504 mg, 2.6 mmol, 1.0 equiv) in DCM (1 mL), a solution of K_2CO_3 (786 mg, 5.7 mmol, 2.2 equiv) in Milli-Q H_2O (4 mL) and a solution of bromoacetyl bromide (270 μL, 3.1 mmol, 1.2 equiv) in DCM (4 mL) were added dropwise at 0 °C. The solution was stirred vigorously at 0 °C. The reaction was equilibrated to 21 °C and continuously stirred at 21 °C for 1 h. The phases were separated, and the organic phase was dried over Na_2SO_4 and concentrated in vacuo. The crude product **1** was obtained as a white solid and used without any further purification (715 mg, acc. to LCMS min. 96, 87%). ^{1}H NMR (500 MHz, $CDCl_3$): δ 7.36−7.28 (m, 7H), 5.11 (s, 2H), 5.05 (dd, J = 43.2, 18.1 Hz, 2H), 3.83 (s, 2H),

https://doi.org/10.1021/acs.jmedchem.1c01054
J. Med. Chem. 2021, 64, 12359−12378

3.44−3.37 (m, 4H). ESI-HRMS: **1**: $C_{12}H_{16}BrN_2O_3^+$ calcd $[M + H]^+$, 315.0346; measured $[M + H]^+$, 315.0337 (Δ = 0.9 ppm).

2,3-Diacetoxybenzoic Acid (2). According to the modified literature procedure from Ferreira,[33] 2,3-dihydroxybenzoic acid (1.29 g, 8.4 mmol, 1.0 equiv) and DMAP (97 mg, 0.8 mmol, 0.1 equiv) were dissolved in tetrahydrofuran (THF) (25 mL). Then, tetraethylammonium (7.0 mL. 50.4 mmol, 6.0 equiv) and Ac_2O (2.4 mL, 25.2 mmol, 3.0 equiv) were added sequentially to the flask. After stirring for 4 h at 29 °C, the solvent was removed via rotary evaporation, and the residue was dissolved in $CHCl_3$ (50 mL) and washed with HCl (0.5 M, 2 × 50 mL). The organic phase was dried over Na_2SO_4 and the solvent was removed in vacuo. Product **2** was dried under high vacuum overnight and obtained as a crude, beige solid (1.73 g, 7.3 mmol, 86%). ^{1}H NMR (500 MHz, $CDCl_3$): δ 7.98 (dd, *J* = 9.4, 3.1 Hz, 1H), 7.48−7.41 (dd, 1H, *J* = 7.9 Hz), 7.36 (t, *J* = 10.2, 5.8 Hz, 1H), 2.34 (s, 3H), 2.33 (d, *J* = 4.3 Hz, 3H). ESI-HRMS: **2**: $C_{11}H_{10}O_6Na^+$ calcd $[M + Na]^+$, 261.0369; measured $[M + Na]^+$, 261.0371 (Δ = 0.2 ppm).

Tri-*tert*-butyl 2,2′,2″-(1,4,7,10-tetraazacyclododecane-1,4,7-triyl)triacetate (3). According to a literature procedure from Ferreira,[33] to a suspension of cyclen (104 mg, 0.6 mmol, 1.0 equiv) and NaOAc (159 mg, 1.9 mmol, 3.3 equiv) in DMA (0.8 mL), a solution of *tert*-butyl-bromoacetate (371 mg, 1.9 mmol, 3.3 equiv) in DMA (1.0 mL, 250 μL/h) was added via a syringe pump. The reaction mixture was stirred for 18 h at 21 °C and a $KHCO_3$ solution (100 mL, 0.5 M in H_2O) was added. The two-phase mixture was extracted with DCM (3 × 50 mL). The combined organic extracts were washed with brine (100 mL) and dried over Na_2SO_4, filtered, and concentrated in vacuo. The obtained clear oil **3** (302 mg, 0.58 mmol, 98%) was used without any further purification. ^{1}H NMR (500 MHz, MeCN-d_3): δ 3.41−3.27 (m, 6H), 2.94 (m, 4H), 2.87−2.75 (m, 12H), 2.16 (br s, 1H), 1.45−1.43 (br s, 27H). ESI-HRMS: **3**: $C_{26}H_{51}N_4O_6^+$ calcd $[M + H]^+$, 515.3802; measured $[M + H]^+$, 515.3820 (Δ = 1.8 ppm).

Tri-*tert*-butyl-2,2′,2″-(10-(2-(((2-(((benzyloxy)carbonyl)amino)ethyl)amino)-2-oxoethyl)-1,4,7,10-tetraazacyclododecane-1,4,7-triyl)triacetate (4). According to a literature procedure from Ferreira,[33] to a suspension of **3** (100 mg, 194 μmol, 1.0 equiv) and K_2CO_3 (111 mg, 803 μmol, 4.1 equiv) in MeCN (3 mL), a solution of **1** in MeCN (1 mL) was added. The reaction was stirred at 22 °C for 1.5 h, and the reaction progress was monitored by LCMS. The suspension was filtered, and the filtrate was concentrated to dryness to obtain a crude, yellow oil of **4** (170 mg), which was employed without further purification in the next step. ^{1}H NMR (500 MHz, MeCN-d_3): δ 8.96 (s, 1H), 7.39−7.33 (m, 5H), 6.17 (s, 1H), 5.03 (s, 2H), 3.25−3.15 (m, 10H), 2.95 (m, 2H), 2.79 (dd, *J* = 15.1, 5.6 Hz, 8H), 2.64 (s, 4H), 2.48 (s, 4H), 1.45−1.40 (br s, 27H) ppm.

Tri-*tert*-butyl-2,2′,2″-(10-(2-((2-aminoethyl)amino)-2-oxoethyl)-1,4,7,10-tetraazacyclododecane-1,4,7-triyl)triacetate (5). Compound **4** (145 mg, 194 μmol, 1.0 equiv) was dissolved in anhydrous MeOH (0.5 mL), degassed with argon balloons, and Pd/C (6 mg, 57 μmol, 0.3 equiv) was added under an argon atmosphere. Subsequently, H_2-filled balloons were inserted into the reaction solution and the reaction was stirred for 2 h at 23 °C. Then, the catalyst was removed by filtration, the filtrate was concentrated to dryness via rotary evaporation, and crude product **5** was obtained as a yellow solid (112 mg, 182 μmol, 92%), which was employed in the next step without further purification. ^{1}H NMR (500 MHz, MeOH-d_4): δ 8.44 (s, 2H), 3.66 (d, *J* = 9.2 Hz, 6H), 3.59 (d, *J* = 11.6 Hz, 2H), 3.50 (t, *J* = 6.0 Hz, 2H), 3.06 (dd, *J* = 13.6, 7.6 Hz, 18H), 1.50 (br s, 27H) ppm. ESI-HRMS: **5**: $C_{30}H_{59}N_6O_7^+$ calcd $[M + H]^+$, 615.4439; measured $[M + H]^+$, 615.4443 (Δ = 0.4 ppm).

Tri-*tert*-butyl-2,2′,2″-(10-(2-((2-(2,3-diacetoxybenzamido)ethyl)amino)-2-oxoethyl)-1,4,7,10-tetraazacyclododecane-1,4,7-triyl)triacetate (6). According to a modified procedure from Ferreira[33] et al., high vacuum-dried **2** (27 mg, 115 μmol, 1.1 equiv) was dissolved in anhydrous DCM/DMF (2/0.2 mL), and oxalylchloride was added at 0 °C (20 μL, 230 μmol, 2.2 equiv) slowly under an argon atmosphere. The resulting reaction was equilibrated to room temperature and continuously stirred for 2 h at 22 °C. The formation of acid chloride was tested via in situ formation of the corresponding methyl ester in anhydrous MeOH and visualization by TLC (PE/EtOAc—1:1). After completion, the solvent was removed, and the residue was dried under high vacuum for a minimum of 2 h or overnight at ambient temperature. Then, a solution of **5** (64 mg, 104 μmol, 1.0 equiv) dissolved in $KHCO_3$ (1 M, 500 μL, pH 8.5−9.0) was cooled to 0 °C before the acid chloride, dissolved in dry 1,4-dioxane (500 μL), was added dropwise under vigorous stirring while the pH was monitored. After the addition, the reaction was continuously stirred for 30 min at 22 °C, and the solvent was removed by rotary evaporation (water bath maximum 30 °C). The residue was dissolved in MeCN/Milli-Q water, filtered over a syringe filter, and purified by RP-HPLC (C18 Phenomenex, 40 min gradient from 10 to 60% MeCN/H_2O 1% AcOH). Product-containing fractions were identified by LCMS and compound **6** (29 mg, 35 μmol, 33%), as well as the mono-acetylated product (5 mg, 6 μmol, 6%) could be obtained as white solids. ^{1}H NMR (700 MHz, MeCN-d_3): δ 7.54 (d, *J* = 7.2 Hz, 1H), 7.36−7.30 (m, 2H), 3.46 (m, 2H), 3.38 (m, 4H), 3.30 (m, 6H), 2.81 (m, 12H), 2.70 (m, 4H), 2.26 (t, *J* = 3.6 Hz, 6H), 1.43 (br s, 27H) ppm. ESI-HRMS: $C_{41}H_{67}N_6O_{12}^+$ calcd $[M + H]^+$, 835.4819; measured $[M + H]^+$, 835.4836 (Δ = 0.17 ppm).

2,2′,2″-(10-(2-((2-(2,3-Diacetoxybenzamido)ethyl)amino)-2-oxoethyl)-1,4,7,10-tetraazacyclododecane-1,4,7-triyl)triacetic Acid (7). To a solution of **6** (22 mg, 26 μmol, 1.0 equiv) in DCM (250 μL) were added AcOH (99%, 250 μL) and TFA (500 μL) at 0 °C. The reaction was stirred for 25 h at 23 °C. The solvent was removed in vacuo, the residue was purified by RP-HPLC (C18 Phenomenex, 40 min gradient: 10−40% MeCN/H_2O 1.0% AcOH), and compound **7** could be obtained as a white solid (4 mg, 6 μmol, 23%). ^{1}H NMR (700 MHz, MeOH-d_4): δ 7.58 (dd, *J* = 7.5, 1.8 Hz, 1H), 7.40−7.33 (m, 2H), 3.86 (m, 4H), 3.76 (m, 2H), 3.71−3.58 (m, 2H), 3.57−3.41 (m, 3H), 3.39−3.32 (m, 6H), 3.30−3.11 (m, 10H), 2.29 (s, 3H), 2.28 (s, 3H). ^{13}C NMR (176 MHz, MeOH-d_4): δ 170.0, 169.9, 168.4, 162.95, 162.7, 144.6, 141.78, 131.8, 127.6, 127.2, 127.0, 119.0, 117.3, 55.8, 40.2, 40.1, 20.5, 20.4. ESI-HRMS: **7**: $C_{29}H_{43}N_6O_{12}^+$ calcd $[M + H]^+$, 667.2932; measured $[M + H]^+$, 667.2938 (Δ = 0.6 ppm).

Gallium-2,2′,2″-(10-(2-((2-(2,3-diacetoxybenzamido)ethyl)amino)-2-oxoethyl)-1,4,7,10-tetraazacyclododecane-1,4,7-triyl)triacetate ([^{nat}Ga]7). Compound **7** (2.8 mg, 4.2 μmol, 1.0 equiv) was dissolved in NaOAc buffer (0.5 M, pH = 4.5, 0.4 mL) and a solution of $^{nat}GaCl_3$ (3.7 mg, 21 μmol, 5.0 equiv) in NaOAc buffer (0.2 mL) was added. The reaction was vortexed for 10 s and then heated to 95 °C for 10 min. Subsequently, [^{nat}Ga]**7** was purified by RP-HPLC (C18 Phenomenex, 40 min gradient 10−30% MeCN/H_2O, 1% AcOH) and could be obtained as a white solid (2.6 mg, 3.5 μmol, 84%). ^{1}H NMR (700 MHz, D_2O): δ 7.55−7.52 (m, 1H), 7.47−7.41 (m, 2H), 4.02−3.94 (m, 2H), 3.87−3.75 (m, 6H), 3.64 (s, 2H), 3.62−3.55 (m, 2H), 3.45 (ddd, *J* = 30.3, 16.8, 9.5 Hz, 8H), 3.34−3.22 (m, 8H), 2.34 (s, 3H), 2.32 (s, 3H) ppm. ^{13}C NMR (176 MHz, D_2O): δ 175.7, 173.4, 172.3, 171.8, 171.3, 168.5, 167.9, 142.3, 139.3, 129.6, 127.6, 126.4, 126.3, 71.3, 66.5, 62.3, 61.6, 59.3, 57.3, 57.1, 54.6, 54.4, 38.9, 38.2, 19.8, 19.0, 16.3 ppm. ESI-HRMS: [^{nat}Ga]**7**: $C_{29}H_{40}GaN_6O_{12}^+$ calcd $[M + H]^+$, 733.1953; measured $[M + H]^+$, 733.1962 (Δ = 0.9 ppm).

2,2′,2″-(10-(2-((2-(2,3-Dihydroxybenzamido)ethyl)amino)-2-oxoethyl)-1,4,7,10-tetraazacyclododecane-1,4,7-triyl)-triacetic Acid (8). To a solution of acetylated compound **7** (44 mg, 70 μmol, 1.0 equiv) in anhydrous MeOH (0.8 mL), cooled to 0 °C, DIPEA (0.2 mL) was added, and the 20% solution was equilibrated to 22 °C and continuously stirred for 4 h. After removal of the solvent and purification by RP-HPLC (C18 Phenomenex, 40 min gradient: 0−20% MeCN/H_2O 0.1% HCOOH) and lyophilization, product **8** could be obtained as a white solid (22 mg, 38 μmol, 60%). ^{1}H NMR (700 MHz, MeOH-d_4): δ 7.37 (dd, *J* = 8.1, 1.4 Hz, 1H), 6.91 (dd, *J* = 7.8, 1.4 Hz, 1H), 6.71 (t, *J* = 8.0 Hz, 1H), 3.75 (s, 4H), 3.59 (s, 2H), 3.55 (t, *J* = 5.8 Hz, 2H), 3.50−3.34 (m, 11H), 3.04 (d, *J* = 29.9 Hz, 8H) ppm. ^{13}C NMR (176 MHz, MeOH-d_4): δ 173.2, 171.1, 170.6, 168.6, 149.2, 145.9, 118.2, 118.1, 117.7, 115.3, 56.1, 55.6, 53.2, 51.1,

https://doi.org/10.1021/acs.jmedchem.1c01054
J. Med. Chem. 2021, 64, 12359−12378

50.6, 48.9, 48.5, 38.7, 38.6 ppm. ESI-HRMS: **8**: $C_{25}H_{39}N_6O_{10}^+$ calcd $[M + H]^+$, 583.2721; measured $[M + MeCN + H]^+$, 583.2713 (Δ = 0.8 ppm). calcd $[M + 2H]^{2+}$, 292.1397; measured $[M + 2H]^{2+}$, 292.1402 (Δ = 0.5 ppm).

Di-*tert*-butyl-(((2,2′-(4-(2-((2-((*tert*-butoxycarbonyl)amino)-ethyl)amino)-2-oxoethyl)-1,4,7,10-tetraazacyclododecane-1,7 diyl)bis(acetyl))bis(azanediyl))bis(ethane-2,1-diyl))-dicarbamate (9a). To a suspension of cyclen (40 mg, 0.23 mmol, 1.0 equiv) and NaOAc (63 mg, 0.77 mmol, 3.3 equiv) in DMA (1 mL) was added a solution of **17** (215 mg, 0.77 mmol, 3.3 equiv) in DMA (1 mL) via a syringe pump (0.25 mL/h). The suspension was stirred for 20 h at 25 °C, and subsequently, a $KHCO_3$ solution was added, and the two-phase solution was extracted with DCM (3 × 100 mL). The combined organic extracts were dried over Na_2SO_4, concentrated to dryness, and **9a** was obtained as a crude, yellow oil (229 mg) and used in the next step without any purification. Compound **9a** was prepared according to a modified literature procedure.[33] ESI-HRMS: 8: calcd $C_{35}H_{69}N_{10}O_9^+$ $[M + H]^+$, 773.5242; measured $[M + H]^+$, 773.5262 (Δ = 2 ppm).

2-(4,7,10-Tris(2-((2-aminoethyl)amino)-2-oxoethyl)-1,4,7,10-tetraaza cyclododecan-1-yl)acetic Acid (9). To a suspension of compound **8** (110 mg, 142 μmol, 1.0 equiv) and K_2CO_3 (39 mg, 284 μmol, 2.0 equiv) in MeCN (0.5 mL) was added *o*-benzyl-bromoacetate (34 μL, 213 μmol, 1.5 equiv) in MeCN (0.5 mL), and the reaction was continuously stirred for 1 h at 28 °C. After completion, the suspension was filtered, and the filtrate was concentrated under reduced pressure. The residue was dissolved in DCM (0.75 mL), and TFA (0.25 mL) was added at 0 °C. The reaction was stirred at ambient temperature for 2 h. Then, the solvent was removed, the residue was dissolved in MeOH (0.5 mL) under a H_2 atmosphere, and Pd/C (3 mg, 25 μmol, 0.17 equiv) was added in Ar-degassed MeOH (0.5 mL) and stirred under a H_2 atmosphere for 1 h at 25 °C. The catalyst was removed over a syringe filter, and the filtrate was evaporated to dryness to yield **9** as a yellow oil (69 mg, 85% pure acc. to LCMS, 99%), which was used without any further purification in the next step. ESI-HRMS: **9**: $C_{22}H_{47}N_{10}O_5^+$ calcd $[M + H]^+$, 531.3724; measured $[M + H]^+$, 531.3736 (Δ = 1.2 ppm).

2-(4,7,10-Tris(2-((2-(2,3-diacetoxybenzamido)ethyl)amino)-2-oxoethyl)-1,4,7,10-tetraazacyclododecan-1-yl)acetic Acid (10). Compound **10** was prepared according to a modified literature procedure.[33] To a solution of **2** (104 mg, 436 μmol) in DCM (400 μL) and DMF (100 μL) was added oxalylchloride (74 μL, 872 μmol) at 0 °C, and the orange solution was stirred at 20 °C for 1 h. Then, the reaction mixture was concentrated and dried under vacuum for 2 h. To a solution of **9** (100 mg, 104 μmol, 1 equiv) in $KHCO_3$ (3.0 mL, 0.5 M in H_2O) was added dropwise a solution of the acid chloride in anhydrous 1,4-dioxane (3.0 mL) at 0 °C over 10 min. After the addition, the mixture was stirred at 20 °C for 0.5 h. After concentration via rotary evaporation at 30 °C, the orange solid was suspended in MeCN with 1% AcOH, filtered, and purified by RP-HPLC (C18 Phenomenex, 40 min-long gradient from 5 to 40% MeCN/H_2O, 1% AcOH). Product-containing fractions were identified by LCMS and lyophilized to yield the white solid **10** (45 mg, 37.8 μmol, 36%). ^{1}H NMR (700 MHz, DMSO-d_6): δ 8.55 (br s, 3H), 8.15 (br s, 3H), 7.49 (dd, J = 12.6, 4.5 Hz, 3H), 7.37−7.33 (m, 6H), 3.59−3.43 (m, 4H), 3.25−2.94 (m, 19H), 2.81 (d, J = 77.4 Hz, 8H), 2.62−2.54 (m, 4H), 2.27 (s, 9H), 2.21 (s, 9H), 1.91 (s, 2H) ppm. ^{13}C NMR (176 MHz, CD_3CN): δ 171.8, 169.8, 169.7, 169.5, 169.4, 166.3, 166.3, 163.0, 144.4, 141.6, 141.6, 140.8, 131.9, 131.7, 127.6, 127.5, 127.4, 127.3, 126.8, 126.6, 62.4, 62.2, 59.2, 57.9, 54.5, 52.8, 51.7, 49.5, 41.3, 40.6, 39.9, 39.7, 21.0, 20.9, 20.9, 20.8 ppm. ESI-HRMS: **10**: $C_{55}H_{72}N_{10}O_{20}^{2+}$ calcd $[M + 2H]^{2+}$, 596.2456; measured $[M + 2H]^{2+}$, 596.2458 (Δ = 0.2 ppm).

2-(4,7,10-Tris(2-((2-(2,3-bis(benzyloxy)benzamido)ethyl)-amino)-2-oxoethyl)-1,4,7,10-tetraazacyclododecan-1-yl)acetic Acid (11a). This compound was prepared according to a modified literature procedure.[33] To a solution of catechol **2** (135 mg, 0.4 mmol, 3.3 equiv) in DCM (1.0 mL) and DMF (0.1 mL) at 0 °C was added oxalylchloride (69 μL, 0.8 mmol, 6.6 equiv), and the solution was stirred for 2 h at 24 °C. The formation of the acid chloride was monitored by TLC (generation of the MeOH ester in dry MeOH and DCM/MeOH 1% running solvent). After completion, the solvent was removed in vacuo and the acid chloride was dried overnight under high vacuum. A solution of amine **9** (65 mg, 0.1 mmol, 1.0 equiv) in $KHCO_3$ (1 M in Milli-Q H_2O, 1 mL) was cooled to 0 °C before the addition of acid chloride of **2** dropwise and dissolved in anhydrous 1,4-dioxane (0.5 mL) at 0 °C. During the addition, the pH was monitored closely. After the addition, the yellow solution was equilibrated to 22 °C and continuously stirred at that temperature for 1 h. Product **11a** was purified by RP-HPLC (C18 Phenomenex, 40 min gradient: 20−85% MeCN/H_2O, 1% AcOH) and could be afforded as a white solid (24 mg, 16 μmol, 13%). ^{1}H NMR (700 MHz, DMSO-d_6): δ 8.52 (br s, 2H), 8.27 (t, 2H), 8.23 (t, 1H), 8.18 (s, 1H), 7.80 (br s, 1H), 7.1−7.5 (m, 39H), 5.18 (d, 6H), 4.99 (d, 6H), 3.0−3.9 (m, 32H), 1.26 (m, 2H) ppm. ^{13}C NMR (176 MHz, DMSO-d_6): δ 166.1, 151.6, 145.2, 137.0, 136.8, 130.80, 128.5, 128.4, 128.3, 128.2, 128.0, 128.0, 127.8, 124.17, 75.16, 70.17 ppm. ESI-HRMS: **11a**: $C_{85}H_{96}N_{10}O_{14}^{2+}$ calcd $[M + 2H]^{2+}$, 740.3548; measured $[M + 2H]^{2+}$, 740.3561 (Δ = 1.3 ppm).

2-(4,7,10-Tris(2-((2-(2,3-dihydroxybenzamido)ethyl)amino)-2-oxoethyl)-1,4,7,10-tetraazacyclododecan-1-yl)acetic Acid (11). This compound was prepared according to a previously established literature procedure.[33] To a solution of **11a** (25 mg, 11 μmol, 1.0 equiv) in Ar-degassed, anhydrous MeOH (0.5 mL) was added Pd/C (3 mg, 3 μmol, 0.17 equiv) in anhydrous, degassed MeOH (0.5 mL). The reaction was stirred under a H_2 atmosphere for 1 h at 22 °C. The catalyst was removed by filtration over a syringe filter, and the reaction was concentrated to dryness to yield **11** (11 mg, 12 μmol, 75%) as a clear oil. Alternatively, the same product could be obtained by a transacetylation procedure: acetylated compound **10** (5 mg, 4 μmol, 1.0 equiv) was stirred in anhydrous MeOH with 20% (v/v) anhydrous DIPEA, added at 0 °C, for 4 h at 25 °C. The solvent and base were removed by rotary evaporation, and the residue was dried overnight under high vacuum to yield **11** as a clear oil (3.94 mg, 4 μmol, quant.) in quantitative yield. ^{1}H NMR (700 MHz, MeOH-d_4): δ 7.21−7.20 (m, 3H), 6.93 (dd, J = 3.9, 2.5 Hz, 3H), 6.72 (m, J = 3.8 Hz, 3H), 3.60−3.51 (m, 12H), 3.35 (d, J = 5.3 Hz, 12H), 3.25−3.16 (m, 12H) ppm. ^{13}C NMR (176 MHz, MeOH-d_4): δ 172.06, 162.37, 162.16, 150.26, 147.55, 120.02, 119.99, 119.94, 119.10, 119.03, 117.08, 117.03, 57.62, 56.44, 40.83, 39.91 ppm. ESI-HRMS: **11**: $C_{43}H_{59}N_{10}O_{14}^+$ calcd $[M + H]^+$, 939.4207; measured $[M + H]^+$, 939.4220 (Δ = 1.3 ppm).

Gallium-(III)-(2-(4,7,10-tris(2-((2-(2,3-dihydroxybenzamido)-ethyl)amino)-2-oxoethyl)-1,4,7,10-tetraazacyclododecan-1-yl)acetate) ([^{nat}Ga]11). To a solution of **11** (11 mg, 12 μmol, 1.0 equiv) in NaOAc buffer (0.5 M, pH = 4.5, 0.5 mL) was added a solution of $GaCl_3$ (10 mg, 59 μmol, 5.0 equiv) in NaOAc buffer (0.2 mL). The components were vortexed for 30 s and heated to 95 °C for 10 min. After 10 and 20 min, additional equivalents of $GaCl_3$ (each 5.0 equiv) were added. The mixture was filtered over a syringe filter and purified via HPLC (40 min gradient: 0−20% MeCN in H_2O with 0.1% TFA) to yield [^{nat}Ga]**11** (2.2 mg, 3.4 μmol, 18%) as a white solid. ^{1}H NMR (700 MHz, MeOH-d_4): δ 7.19−7.14 (m, 3H), 6.94−6.92 (m, 3H), 6.73−6.69 (m, 3H), 3.91−3.83 (m, 6H), 3.81 (d, J = 16.4 Hz, 2H), 3.75−3.71 (m, 2H), 3.69 (d, J = 16.4 Hz, 2H), 3.67−3.63 (m, 2H), 3.50 (m, J = 17.8, 13.2, 7.2, 3.3 Hz, 8H), 3.42−3.36 (m, 8H), 3.29−3.08 (m, 6H) ppm. ^{13}C NMR (176 MHz, MeOH-d_4): δ 174.07, 173.84, 172.70, 172.11, 172.05, 168.93, 162.34, 162.14, 150.16, 149.23, 147.31, 147.25, 120.06, 119.91, 119.85, 119.36, 118.77, 118.64, 117.31, 117.00, 116.70, 60.93, 57.90, 57.48, 56.00, 55.42, 49.00, 46.97, 43.94, 43.49, 40.63, 39.92, 38.39, 28.12, 17.34, 17.17.

***N*-(2-(2-(2-(2-Azidoethoxy)ethoxy)ethoxy)ethyl)-2-bromoacetamide (12).** Amino PEG_3 azide linker (550 mg, 2.52 mmol, 1.0 equiv) was dissolved in 100 mL of DCM at 0 °C. Then, K_2CO_3 (417.95 mg, 3.05 mmol, 1.2 equiv) dissolved in H_2O (50 mL) was added in one portion. Bromoacetyl bromide (610 mg, 3.02 mmol, 1.2 equiv) was dissolved in DCM (25 mL) and added dropwise at 0 °C. After stirring for 15 min at 0 °C, the ice bath was removed, and the two-phase solution was continuously stirred for 1 h at 23 °C. The phases were separated, and the aqueous phase was extracted with

https://doi.org/10.1021/acs.jmedchem.1c01054
J. Med. Chem. 2021, 64, 12359−12378

DCM (2 × 40 mL). The combined organic extracts were dried over Na_2SO_4 and concentrated in vacuo. The residue was dried under high vacuum overnight, yielding **12** as a slightly yellow oil (773.36 mg, 2.29 mmol, 91%), which was used without further purification in the next step. ^{1}H NMR (500 MHz, $CDCl_3$): δ 6.91 (br s, 1H), 3.87 (s, 2H), 3.67 (m, 10 H), 3.59 (t, 2H), 3.49 (m, 2H), 3.39 (m, 2H) ppm. ^{13}C NMR (100 MHz, $CDCl_3$): δ 165.7, 70.9, 70.8, 70.6, 70.2, 69.5, 53.6, 50.8, 40.1, 29.3 ppm. ESI-HRMS: **12**: $C_{10}H_{20}BrN_4O_4^+$ calcd $[M + H]^+$, 339.0662; measured $[M + H]^+$, 339.0663 (Δ = 0.1 ppm).

2,2′,2″-(10-(14-Azido-2-oxo-6,9,12-trioxa-3-azatetradecyl)-1,4,7,10-tetraazacyclododecane-1,4,7-triyl)tris(*N*-(2-aminoethyl)acetamide) (13). This compound was prepared according to a modified literature procedure.[33] Linker **12** (302 mg, 0.89 mmol, 1.15 equiv) was dissolved in MeCN (2.5 mL) and added to a stirred suspension of **9a** (600 mg, 0.776 mmol, 1.0 equiv) and K_2CO_3 (429 mg, 3.11 mmol, 4.0 equiv) in MeCN (7.5 mL). The reaction was continuously stirred overnight at 22 °C. The reaction progress was monitored by LCMS, and after full conversion, the reaction mixture was filtered and dried for 1 h in vacuo to obtain a crude beige solid. The residue was dissolved in DCM (75 mL) and washed with water and brine (each 2 × 50 mL) and then dried over Na_2SO_4. The solvent was removed by rotary evaporation, and the residue was dried under high vacuum for 30 min. Then, DCM (5 mL) and TFA (4 mL) were added at 0 °C, and the reaction was equilibrated to room temperature and continuously stirred at 24 °C for 3 h. After full conversion, the solvent was removed by rotary evaporation, the residue was dried overnight under high vacuum, and crude **13** (229 mg, 0.313 mmol, 40% over two steps) was obtained as a beige oil. ^{1}H NMR (MeOH-d_4, 700 MHz): δ 4.57 (s, 4H), 3.68 (m, 8H), 3.62 (m, 2H), 3.52 (t, J = 4.9 Hz, 2H), 3.41 (t, J = 5.5 Hz, 2H), 3.16 (m, J = 6.4 Hz, 8H), 3.07 (t, J = 5.9 Hz, 8H), 3.06 (s, 4H), 2.92 (s, 4H), 2.15 (s, 4H), 2.08 (s, 4H) ppm.

***N*,*N*′,*N*″-(((2,2′,2″-(10-(2-Oxo-14-(1l2,3l2-triaz-2-en-1-yl)-6,9,12-trioxa-3-azatetradecyl)-1,4,7,10-tetraazacyclododecane-1,4,7triyl)tris(acetyl))tris(azanediyl))tris(ethane-2,1-diyl))tris(2,3-dihydroxybenzamide) (14).** Oxalylchloride (250 μL, 2.92 mmol, 9.0 equiv) was added to a stirred solution of **2** (386 mg, 1.62 mg, 5.0 equiv) in dry DCM/DMF (500 μL/50 μL) at 0 °C under Ar conditions. The suspension was stirred for 2 h at 22 °C, and the reaction progress was checked by TLC. Subsequently, the solvent was removed by rotary evaporation, and the residue was dried under high vacuum overnight to yield a dark brown solid. 1,4-Dioxane (1.2 mL) was added, and the suspension was added dropwise to a solution of **13** (237 mg, 0.32 μmol, 1.0 equiv) in 1 M K_2CO_3 on ice. The pH was kept constant by addition of minute amounts of sat. K_2CO_3 solution when required. The reaction mixture was equilibrated to 23 °C and continuously stirred for 1 h at that temperature. Subsequently, the mixture was extracted with DCM (3 × 100 mL), the combined organic extracts were dried over Na_2SO_4, and the solvent was removed in vacuo. The residue was taken up in MeCN/H_2O 1:1 (2.5 mL) and purified by RP-HPLC (C18 Phenomenex, 40 min gradient 0−35% MeCN/H_2O 1% AcOH). Product-containing fractions were identified by LCMS and lyophilized to obtain **14** (175 mg, 0.126 mmol, 39%) as a white solid. ^{1}H NMR (500 MHz, MeOH-d_4): δ 7.48 (m, 3H), 7.36−7.31 (m, 6H), 3.68−3.59 (m, 16H), 3.58−3.56 (m, 2H), 3.53−3.50 (m, 2H), 3.48−3.46 (m, 4H), 3.38 (m, 12H), 3.05−2.73 (m, 16H), 2.30−2.28 (m, 9H), 2.27−2.25 (m, 9H) ppm. ^{13}C NMR (176 MHz, MeOH-d_4): δ 180.2, 175.2, 172.2, 171.9, 163.1, 162.9, 151.3, 148.5, 147.2, 130.7, 129.0, 121.7, 121.2, 120.8, 120.0, 119.3, 119.2, 119.1, 118.3, 117.9, 117.4, 117.2, 117.1, 113.9, 71.7, 71.6, 71.6, 71.6, 71.5, 71.3, 71.2, 71.1, 71.1, 70.5, 70.4, 66.9, 66.1, 62.6, 57.5, 54.5, 54.1, 52.8, 51.8, 49.0, 43.0, 40.2, 39.9, 39.7, 39.5, 24.2, 20.7, 19.8, 18.6, 17.8, 17.4, 17.3, 17.2, 14.0, 10.6 ppm. ESI-HRMS: **14**: $C_{63}H_{87}N_{14}O_{22}^+$ calcd $[M + H]^+$, = 1391.6113; measured $[M + H]^+$, 1391.6165 (Δ = 5.2 ppm).

2,2′,2″-(10-(2-Oxo-2-((2-(((((5a*R*,6a*S*)-1-(2-oxo-1-(4,7,10-tris(2-((2-(2,3-dihydroxybenzamido)ethyl)amino)-2-oxoethyl)-1,4,7,10-tetraazacyclododecan-1-yl)-6,9,12-trioxa-3-azatetradecan-14-yl)-1,4,5,5a,6,6a,7,8-octahydrocyclopropa[5,6]cycloocta[1,2-*d*][1,2,3]triazol-6yl)methoxy)carbonyl)amino)ethyl)amino)ethyl)-1,4,7,10-tetraazacyclododecane-1,4,7-triyl)triacetic Acid (15). Azido DOTAM **14** (30 mg, 0.02 mmol, 1.0 equiv) was dissolved in MeOH (800 μL) and DIPEA (200 μL) was added at 0 °C. The ice bath was removed, the reaction was stirred for 4 h at 25 °C, and then the solvent was removed by rotary evaporation. The residue was dried under high vacuum overnight to remove residual DIPEA to yield a beige oil. A mixture of 1× PBS (pH 7.4)/DMSO (300 μL each) and BCN-DOTA (20.14 mg, 0.03 mmol, 1.5 equiv) in 400 μL of MeOH were added. The reaction was stirred overnight at 25 °C, and the reaction progress was controlled by LCMS. After completion, the organic solvent was removed as much as possible by rotary evaporation. The residual liquid was filtered and injected into the RP-HPLC (C18 Phenomenex, 40 min gradient 0−30% MeCN/H_2O 0.1% HCOOH). Product-containing fractions were identified by LCMS and lyophilized to dryness to yield **15** (30 mg, 0.02 mmol, 80%) as a colorless oil. ^{1}H NMR (700 MHz, DMSO-d_6): δ 13.12−12.19 (br s, 1H), 9.53−9.07 (s, 1H), 8.85 (d, J = 17.4 Hz, 3H), 8.19 (m, 6H), 7.69 (m, 1H), 7.43 (m, 1H), 7.26 (d, J = 8.0 Hz, 3H), 6.92−6.89 (m, 3H), 6.65 (dd, J = 11.3, 4.5 Hz, 3H), 4.40−4.37 (m, 2H), 4.05−3.99 (m, 2H), 3.79 (m, 2H), 3.72 (m, 2H), 3.56−3.51 (m, 4H), 3.49 (m, 4H), 3.48−3.46 (m, 4H), 3.46−3.44 (m, 8H), 3.42 (m, 6H), 3.39−3.37 (m, 8H), 3.34 (m, 4H), 3.30 (dd, J = 5.5 Hz, 8H), 3.25 (dd, J = 10.1, 4.4 Hz, 4H), 3.16−3.14 (m, 2H), 3.11 (s, 2H), 3.01−2.95 (m, 14H), 2.84 (br s, 8H), 2.76−2.72 (m, 2H), 2.67 (m, 4H), 2.12−2.05 (m, 2H), 1.56−1.50 (m, 2H), 1.09 (dd, J = 16.8, 8.4 Hz, 1H), 0.91−0.89 (m, 1H) ppm. ^{13}C NMR (176 MHz, DMSO-d_6): δ 181.3, 181.2, 179.4, 172.6, 165.9, 159.1, 155.7, 155.7, 152.7, 143.3, 128.3, 127.4, 126.7, 124.5, 124.5, 79.5, 79.2, 79.2, 79.1, 78.9, 78.8, 78.8, 78.7, 78.4, 78.4, 78.3, 70.9, 70.8, 65.7, 64.5, 64.3, 64.2, 60.5, 59.8, 59.5, 59.3, 56.7, 48.3, 48.2, 47.9, 47.6, 47.3, 34.8, 31.7, 31.4, 30.7, 28.6, 28.1, 26.8, 9.6 ppm. ESI-HRMS: **15**: $C_{80}H_{122}N_{20}O_{25}^{2+}$ calcd $[M + 2H]^{2+}$, 881.4439; measured $[M + 2H]^{2+}$, 881.4325 (Δ = 1.4 ppm).

Gallium-2,2′,2″-(10-(2-oxo-2-((2-(((((5a*R*,6a*S*)-1-(2-oxo-1-(4,7,10-tris(2-((2-(2,3-dihydroxybenzamido)ethyl)amino)-2-oxoethyl)-1,4,7,10-tetraazacyclododecan-1-yl)-6,9,12-trioxa-3-azatetradecan-14-yl)-1,4,5,5a,6,6a,7,8-octahydrocyclopropa[5,6]cycloocta[1,2-*d*][1,2,3]triazol 6yl)-methoxy)carbonyl)amino)ethyl)amino)ethyl)-1,4,7,10-tetraazacyclododecane-1,4,7-triyl)triacetate ([^{nat}Ga]15). **15** (10 mg, 0.006 mmol, 1.0 equiv) was dissolved in 200 μL of DMSO, and $^{nat}GaCl_3$ (2 mg, 0.011 mmol, 2 equiv), dissolved in NaOAc buffer, was added at 23 °C. The reaction was heated to 100 °C under vigorous stirring. The complexation progress was monitored by LCMS—after full conversion (ca. 10 min), the solution was filtered and subsequently injected into RP-HPLC (C18 Phenomenex, 40 min gradient 2−30% MeCN/H_2O, 0.1% HCOOH). Product-containing fractions were identified by LCMS and lyophilized to dryness, yielding the complex [^{nat}Ga]**15** as a white solid (7.9 mg, 0.004 mmol, 76%). H NMR (700 MHz, MeOH-d_4): δ 7.34−7.07 (dd, J = 7.8, 1.3 Hz, 3H), 6.93 (dd, J = 7.8, 1.3 Hz, 3H), 6.79−6.63 (t, J = 8.3 Hz, 3H), 3.66−3.61 (m, 24H), 3.60−3.58 (m, 4H), 3.57−3.53 (q, 8H), 3.48−3.43 (t, J = 5.96 Hz, 8H), 3.41 (m, 8H), 3.38−3.35 (t, J = 5.96 Hz, 8H), 2.94 (m, 28H), 2.21 (m, 1H), 1.61 (m, 1H), 1.08 (m, 1H) ppm. C NMR (176 MHz, MeOH-d_4): δ 171.83, 169.47, 150.38, 147.50, 119.76, 119.70, 118.76, 116.77, 71.61, 71.56, 71.50, 71.26, 71.07, 70.38, 58.29, 57.72, 57.48, 53.18, 52.89, 51.77, 49.00, 40.39, 40.17, 40.13, 17.28 ppm.

Benzyl (*R*)-2-Bromopropanoate (16). Compound **16** was prepared according to a literature procedure from Mao et al.[64] To a solution of (*R*)-2-bromo-propionic acid (400 mg, 2.61 mmol, 1.0 equiv) and DCC (648 mg, 3.14 mmol, 1.2 equiv) in Et_2O (5 mL), a solution of DMAP (16 mg, 0.13 mmol, 0.05 equiv) and BnOH (326 μL, 3.14 mmol, 1.2 equiv) in Et_2O (2 mL) was added, and the reaction was stirred overnight. The next morning, the reaction was concentrated in vacuo and **16** (528 mg, 2.17 mmol, 83%) could be obtained via silica gel chromatography (0−1% EtOAc in PE bp 40−60 °C) as a colorless oil. ^{1}H NMR (500 MHz, $CDCl_3$): δ 7.39−7.32 (m, 5H), 5.21 (t, J = 2.0 Hz, 2H), 4.45−4.38 (m, 1H), 1.84 (d, J = 6.9 Hz, 3H) ppm.

https://doi.org/10.1021/acs.jmedchem.1c01054
J. Med. Chem. 2021, 64, 12359−12378

***tert*-Butyl(2-(2-bromoacetamido)ethyl)carbamate (17).** According to a literature procedure from Ferreira[33] et al., to a solution of *N*-Boc-ethylendiamine (4.0 mL, 25 mmol, 1.0 equiv) in DCM (120 mL), a solution of K_2CO_3 (4.2 g, 30 mmol, 1.2 equiv) in H_2O (90 mL) was added, and the two-phase mixture was cooled to 0 °C. A solution of bromoacetyl bromide (2.6 mL, 30 mmol, 1.2 equiv) in DCM (90 mL) was added dropwise over 30 min at 0 °C, and the reaction mixture was stirred for 1.5 h at 21 °C. The phases were separated, and the aqueous phase was extracted with DCM (3 × 100 mL). The organic extracts were washed with H_2O (2 × 200 mL) and brine (2 × 100 mL) and dried over Na_2SO_4. After removal of the solvent, product **17** was obtained as a white solid (6.5 g, 23 mmol, 93%), which was used as a crude in the next step. ^{1}H NMR (500 MHz, $CDCl_3$): δ 7.09 (s, 1H), 4.87 (s, 1H), 3.86 (s, 2H), 3.42−3.37 (m, 2H), 3.34−3.29 (m, 2H), 1.45 (s, 9H) ppm. ^{13}C NMR (176 MHz, $CDCl_3$): δ 166.5, 79.9, 41.4, 39.8 28.4 ppm. ESI-HRMS: **17**: $C_9H_{18}BrN_2O_3^+$ calcd $[M + H]^+$, 281.0494; measured $[M + H]^+$, 281.0502 (Δ = 0.8 ppm).

Dibenzyl-2,2′-(1,4,7,10-tetraazacyclododecane-1,7-diyl)-(2*S*,2′*S*)-dipropionate (18), Dibenzyl-2,2′-(1,4,7,10-tetraazacyclododecane-1,4-diyl)(2*S*,2′*S*)-dipropionate (19), and Tribenzyl-2,2′,2″-(1,4,7,10-tetraazacyclododecane-1,4,7-triyl)-(2*S*,2′*S*,2″*S*)-tripropionate (20). To a suspension of cyclen (50 mg, 0.29 mmol, 1.0 equiv) and NaOAc (79 mg, 0.96 mmol, 3.3 equiv) in DMA (0.5 mL), a solution of **16** (233 mg, 0.96 mmol, 3.3 equiv) in DMA (1.0 mL) was added via a syringe pump (300 μL/h). The suspension was stirred for 20 h at 28 °C, washed with $KHCO_3$ solution (2 × 50 mL, 0.5 M), and extracted with $CHCl_3$ (3 × 50 mL). The combined organic extracts were dried over Na_2SO_4, and the solvent was removed under reduced pressure. Products were obtained as an inseparable mixture of di- (**18**/**19**) and tri-substituted (**20**) compounds (180 mg), respectively, and employed in the next step without purification. LCMS: **18**/**19**: m/z = 497.66 $[M + H]^+$, t_R = 0.53 min. **20**: m/z = 659.85 $[M + H]^+$; t_R = 0.99 min.

Dibenzyl-2,2′-(4,10-bis(2-((2-aminoethyl)amino)-2-oxoethyl)-1,4,7,10-tetraazacyclododecane-1,7-diyl)(2*S*,2′*S*)-dipropionate (21), Dibenzyl-2,2′-(7,10-bis(2-((2-aminoethyl)amino)-2-oxoethyl)-1,4,7,10-tetraazacyclododecane-1,4-diyl)(2*S*,2′*S*)-dipropionate (22), and Tribenzyl-2,2′,2″-(10-(2-((2-aminoethyl)-amino)-2-oxoethyl)-1,4,7,10-tetraazacyclododecane-1,4,7-triyl)(2*S*,2′*S*,2″*S*)-tripropionate (23). To a suspension of **18**, **19**, and **20** (142 mg, ca. 0.22 mmol, 1.0 equiv) and K_2CO_3 (149 mg, 1.08 mmol, 5.0 equiv) in MeCN (1.5 mL), **17** (182 mg, 0.65 mmol, 3.0 equiv) was added in MeCN (0.5 mL), and the suspension was stirred for 1 h at 28 °C. The reaction was filtered, the solvent was removed and dried under reduced pressure, and the crude mixture was separated by RP-HPLC (C18 Phenomenex, 40 min gradient, 10−60% MeCN/H_2O, 0.1% HCOOH). A mixture of **21**/**22** (21 mg, 0.023 mmol, 11%) was obtained as a white solid. Several attempts to separate the regioisomers **21**/**22** by RP-HPLC failed. In addition, pure **23** (25 mg, 0.0291 mmol, 13%) was obtained as a white solid. **21**/**22**: ^{1}H NMR (500 MHz, DMSO-d_6): δ 7.36 (m, 10H), 5.11 (s, 4H), 5.09 (s, 2H), 3.62 (m, J = 17.2 Hz, 2H), 3.62 (m, J = 55.3 Hz, 2H), 3.53 (m, 4H), 3.12 (m, 2H), 2.95 (m, 10H), 2.76 (m, 12 H), 1.36 (s, 6H), 1.33 (s, 18H) ppm. ESI-HRMS: **21**/**22**: $C_{46}H_{73}N_8O_{10}^+$ calcd $[M + H]^+$, 897.5443; measured $[M + H]^+$, 897.5456 (Δ = 1.3 ppm). **23**: ^{1}H NMR (500 MHz, DMSO-d_6): δ 7.36−7.33 (m, 15H), 5.14 (s, J = 2.8 Hz, 2H), 5.10 (s, J = 1.5 Hz, 2H), 5.09 (s, 2H), 3.47−3.43 (m, 2H), 3.25−3.16 (m, 2H), 3.10 (m, J = 12.5, 6.3 Hz, 2H), 3.04−2.99 (m, 2H), 2.96 (m, J = 5.9 Hz, 2H), 2.82 (m, 2H), 2.76 (m, J = 14.7 Hz, 2H), 2.69 (m, J = 4.2 Hz, 4H), 2.66 (m, 4H), 1.34 (s, 9H), 1.02 (m, J = 6.8 Hz, 6H) ppm. ^{13}C NMR (176 MHz, DMSO-d_6): δ 173.2, 173.2, 170.9, 170.9, 170.9, 170.9, 168.5, 168.5, 166.8, 163.0, 155.6, 154.9, 154.9, 136.1, 136.1, 136.0, 136.0, 135.6, 135.6, 128.4, 128.4, 128.1, 128.1, 128.0, 128.0, 127.9, 127.9, 127.9, 127.9, 77.6, 77.6, 65.8, 65.8, 65.2, 65.2, 61.1, 61.0, 55.5, 53.7, 53.7, 52.9, 52.3, 52.1, 51.3, 51.3, 49.6, 49.0, 48.6, 47.3, 46.91, 39.5, 38.5, 38.5, 28.1, 28.1, 11.8, 11.4 ppm.

Tribenzyl-2,2′,2″-(10-(2-((2-(2,3-diacetoxybenzamido)-ethyl)amino)-2-oxoethyl)-1,4,7,10-tetraazacyclododecane-1,4,7-triyl)(2*S*,2′*S*,2″*S*)-tripropionate (24a). **23** (21 mg, 24 μmol, 1.0 equiv) was dissolved in DCM (0.75 mL), and TFA was added at 0 °C (0.25 mL). The solution was continuously stirred for 2 h at 28 °C. After completion, the reaction was concentrated to dryness and dried under HV overnight to yield **23a** as a clear oil (18.6 mg, 24 μmol, quant.). To a solution of **2** (6 mg, 26 μmol, 1.1 equiv) in DCM (200 μL) and DMF (50 μL), oxalylchloride (5 μL, 57 μmol, 2.2 equiv) was added at 0 °C, and the reaction was stirred for 2 h at 22 °C. The formation of the acid chloride was monitored as previously described. After removal of the solvent, the acid chloride was dried under high vacuum. A solution of **23a** (21 mg, 24 μmol, 1.0 equiv) in $KHCO_3$ (1 M, 0.5 mL) was cooled to 0 °C before the acid chloride was added dropwise in 1,4-dioxane (0.1 mL) while monitoring the pH staying in a range of 8.5−9. The resulting beige solution was stirred for 30 min at 22 °C, and the solvent was removed by rotary evaporation at a maximum 30 °C water bath temperature. The residue was dissolved in DCM (50 mL) and washed with sat. $NaHCO_3$ solution and water (each 3 × 50 mL), and the organic phase was dried over Na_2SO_4. The solvent was removed in vacuo, and the residue dried overnight under high vacuum, yielding crude product **24a** as a clear oil (2.5 mg, 3 μmol, 12%). LCMS: m/z = 979.45 $[M + H]^+$; t_R = 1.35 min. ESI-HRMS: **23a**: $C_{42}H_{59}N_6O_7^+$ calcd $[M + H]^+$, 759.4439; measured $[M + H]^+$, 759.4454 (Δ = 1.5 ppm). ^{1}H NMR (700 MHz, MeOH-d_4): δ 7.45−7.33 (m, 18H), 5.14 (m, 6H), 3.64 (m, 2H), 3.48−3.43 (m, 2H), 3.07 (m, 3H), 3.07 (s, 3H), 2.95 (m, 0.91) (s, 3H), 2.28−2.22 (m, 8H), 2.22−2.19 (m, 4H), 1.72−1.70 (d, 3H), 1.52−1.34 (m, 6H) ppm.

(2*S*,2′*S*,2″*S*)-2,2′,2″-(10-(2-((2-(2,3-Dihydroxybenzamido)-ethyl)amino)-2-oxoethyl)-1,4,7,10-tetraazacyclododecane-1,4,7-triyl)tripropionic Acid (24). To a solution of **24a** (6.5 mg, 7 μmol, 1.0 equiv) in Ar-degassed, anhydrous MeOH (0.5 mL), Pd/C (0.1 mg, 1.2 μmol, 0.17) was added. The suspension was stirred for 1 h under a H_2 atmosphere at 22 °C. The catalyst was removed by filtration over a syringe filter, and the solvent was removed under reduced pressure. The solid was taken up in MeOH (0.8 mL) and DIPEA (0.2 mL) was added at 0 °C. The solution was stirred for 1 h at 22 °C and concentrated to dryness. HPLC purification of the product mixture (C18 Phenomenex, 40 min gradient 0−30% MeCN/H_2O, 0.1% TFA) yielded **24** (2.5 mg, 4 μmol, 57%) as a white solid. ^{1}H NMR (700 MHz, MeOH-d_4): δ 7.25−7.20 (m, 1H), 6.94 (m, 2H), 6.74 (m, 2H), 4.01−3.36 (m, 17H), 3.21−3.01 (m, 8H), 1.54 (d, 3H), 1.42−1.36 (d, 3H), 1.33−1.28 (d, 3H). ESI-HRMS: **24**: $C_{28}H_{45}N_6O_{10}^+$ calcd $[M + H]^+$, 625.3191; measured $[M + H]^+$, 625.3199 (Δ = 0.8 ppm).

(((((2,2′-(4,10-Bis((*S*)-1-(benzyloxy)-1-oxopropan-2-yl)-1,4,7,10-tetraazacyclododecane-1,7-diyl)bis(acetyl))bis-(azanediyl))bis(ethane-2,1-diyl))bis(azanediyl))bis(carbonyl))-bis(benzene-3,1,2-triyl)tetraacetate (25a) and (((((2,2′-(7,10-bis((*S*)-1-(benzyloxy)-1-oxopropan-2-yl)-1,4,7,10-tetraazacyclododecane-1,4-diyl)bis(acetyl))bis(azanediyl))bis(ethane-2,1-diyl))bis(azanediyl))bis(carbonyl)) bis(benzene-3,1,2-triyl)-tetraacetate (26a). **21**/**22** (21 mg, 23 μmol, 1 equiv) was dissolved in DCM (0.75 mL), and TFA was added at 0 °C (0.25 mL). The solution was continuously stirred for 2 h at 28 °C, then concentrated to dryness, and dried under HV overnight to yield a clear oil (18.7 mg, 23 μmol, quant.). To a solution of **2** (11 mg, 50 μmol, 2.2 equiv) in DCM (500 μL) and DMF (50 μL), oxalylchloride (18.9 μL, 101.2 μmol, 4.4 equiv) was added at 0 °C, and the solution was stirred for 1 h at 22 °C. The formation of the acid chloride was monitored as previously described. After removal of the solvent, the acid chloride was dried under high vacuum for at least 1 h. A solution of **21a** and **22a** (18.7 mg, 23 μmol, 1.0 equiv) in $KHCO_3$ (1 M in Milli-Q water, 1 mL) was cooled to 0 °C, and the acid chloride was added dropwise in anhydrous 1,4-dioxane (0.1 mL) while monitoring the pH to stay in the range of 8.5−9. The resulting yellow solution was stirred for 30 min at 22 °C, and the solvent was removed under reduced pressure at a maximum 30 °C water bath temperature. The residue was dissolved in DCM (50 mL) and washed with sat. $NaHCO_3$, water (each 3 × 50 mL), and dried over Na_2SO_4. The solvent was removed in vacuo and dried overnight at ambient temperature, yielding the product **25a**/**26a** (24.33 mg, 21.4 μmol, 93%) as a clear oil. The crude was employed without further purification in the next step. LCMS: m/z = 1138.34

https://doi.org/10.1021/acs.jmedchem.1c01054
J. Med. Chem. 2021, 64, 12359−12378

[M + H$^+$]; t_R = 1.22 min. ESI-HRMS: **21a**/**22a** $C_{36}H_{57}N_8O_6^+$ calcd [M + H]$^+$, 697.4395; measured [M + H]$^+$, 697.4402 (Δ = 0.7 ppm). ^{1}H NMR (700 MHz, DMSO-d_6): δ 8.53−8.19 (m, 4H), 7.47 (m, 2H), 7.43−7.29 (m, 16H), 5.14−5.08 (m, 4H), 3.83−3.53 (m, 7H), 3.39 (m, 2H), 3.32−3.23 (m, 8H), 2.4−3.2 (m, 6H), 2.67−3.2 (m, 15H), 2.22−2.16 (s, 6H), 1.36 (s, 1H), 1.29−1.21 (m, 6H) ppm.

(2*S*,2′*S*)-2,2′-(4,10-Bis(2-((2-(2,3-dihydroxybenzamido)ethyl)amino)-2-oxoethyl)-1,4,7,10-tetraazacyclododecane-1,7-diyl)dipropionic Acid (25) and (2*S*,2′*S*)-2,2′-(7,10-Bis(2-((2-(2,3-dihydroxybenzamido)ethyl)amino)-2-oxoethyl)-1,4,7,10-tetraazacyclododecane-1,4-diyl)dipropionic Acid (26). To a solution of **25a**/**26a** (50 mg, 44 μmol, 1.0 equiv) in anhydrous MeOH under an Ar atmosphere (0.5 mL), Pd/C (0.8 mg, 0.7 μmol, 0.17 equiv) was added in Ar-degassed MeOH (0.5 mL). The reaction was continuously stirred for 2 h at 22 °C under a H_2 atmosphere. The mixture was filtered, and the solvent was removed under reduced pressure. The residue was dissolved in MeOH (0.8 mL), and DIPEA (0.2 mL) was added at 0 °C. The reaction was stirred for 1 h at 23 °C, and the solvent was evaporated to dryness. The residue was purified by RP-HPLC (C18 Phenomenex, 40 min gradient, 10−30% MeCN/H_2O, 0.1% TFA). **25**/**26** could not be separated, and a mixture of **25**/**26** (1.2 mg, 1.5 μmol, 3%) was obtained as a white solid. ^{1}H NMR (700 MHz, DMSO-d_6): δ 9.02 (d, *J* = 64.0 Hz, 3H), 8.24−7.86 (m, 2H), 7.49−7.19 (s, 2H), 6.88 (m, 2H), 6.65 (m, 2H), 3.6 (s, 2H), 3.40 (m, 4H), 3.25−2.62 (m, 19H), 2.21 (s, 1H), 2.08 (d, *J* = 8.4 Hz, 2H), 1.24−1.12 (m, 6H) ppm. ESI-HRMS: 25/26: $C_{36}H_{53}N_8O_{12}^+$ calcd [M + H]$^+$, 789.3785; measured [M + H]$^+$, 789.3788 (Δ = 0.3 ppm).

***tert*-Butyl (*R*)-(2-(2-Bromopropanamido)ethyl)carbamate (27).** The product was prepared according to a literature procedure from Moore et al.[65] (*R*)-2-Bromo-propanoic acid (168 mg, 1.1 mmol, 1.1 equiv) and HATU (380 mg, 1.0 mmol, 1.0 equiv) were suspended in DCM (3 mL) and DMF (0.75 mL) and stirred for 5 min at 21 °C. Then, *N*-boc-ethylendiamine (158 μL, 1.0 mmol, 1.0 equiv) and DIPEA (170 μL, 1.0 mmol, 1.0 equiv) were added slowly subsequently to the reaction mixture and continuously stirred for 4 h at 25 °C. The solvent was removed under reduced pressure. The residue was taken up in EA (20 mL) and washed with HCl (pH = 3, 2 × 15 mL), sat. $NaHCO_3$ (2 × 15 mL), and brine (15 mL). The organic phase was dried over Na_2SO_4 and the solvent was removed in vacuo. Product **27** was obtained as a white solid (318 mg, 1.07 μmol, 97%) and used directly in the next step. ^{1}H NMR (500 MHz, $CDCl_3$): δ 7.00 (br s, 1H), 4.86 (br s, 1H), 4.38 (q, *J* = 7.0 Hz, 1H), 3.40−3.35 (m, 2H), 3.32 (d, *J* = 5.6 Hz, 2H), 1.87 (d, *J* = 7.1 Hz, 3H), 1.45 (s, 9H) ppm. ^{13}C NMR (176 MHz, $CDCl_3$): δ 170.2, 157.1, 80.1, 44.9, 41.8, 39.9, 28.5, 23.2 ppm.

Di-*tert*-butyl-((((2*S*,2′*S*)-2,2′-(1,4,7,10-tetraazacyclododecane-1,7-diyl)bis(propanoyl))bis(azanediyl))bis(ethane-2,1-diyl))dicarbamate (29), Di-*tert*-butyl-((((2*S*,2′*S*)-2,2′-(1,4,7,10-tetraazacyclododecane-1,4-diyl)bis(propanoyl))bis(azanediyl))bis(ethane-2,1-diyl))dicarbamate (30), and Di-*tert*-butyl-((((2*S*,2′*S*)-2,2′-(4-((*S*)-1-((2-((tertbutoxycarbonyl)amino)ethyl)amino)-1-oxopropan-2-yl)-1,4,7,10-tetraazacyclododecane-1,7-diyl)bis(propanoyl))bis(azanediyl))bis(ethane-2,1-diyl))dicarbamate (31). To a suspension of cyclen (16 mg, 93 μmol, 1.0 equiv) and NaOAc (25 mg, 308 μmol, 3.3 equiv) in MeCN (1 mL) was added a solution of (*R*)-**27** (91 mg, 308 μmol, 3.3 equiv) at 22 °C in DMA (1 mL) *via* a syringe pump (0.25 mL/h). The suspension was stirred for 72 h at 25 °C, filtered, and the solvent was removed under reduced pressure. The residue was dissolved in MeCN (0.5 mL), and K_2CO_3 (100 mg, 723 μmol) was added. Then, a solution of *O*-benzyl bromoacetate (31 μL, 198 μmol, 4.4 equiv) in MeCN (0.5 mL) was added, and the mixture was stirred for 1 h at 22 °C. The mixture was filtered, and the reaction concentrated in vacuo and **29**/**30** (27 mg, 45 μmol, 48%) as well as the tri-substitution **31** (7 mg, 8 μmol, 9%) were obtained as a clear oil. Compound **29**/**30** could not be separated by multiple RP-HPLC attempts and were employed like this in the next step. **29**/**30**: ^{1}H NMR (500 MHz, DMSO-d_6): δ 7.50−7.19 (m, 10H), 5.14−5.07 (s, 4H), 3.32 (m, 4H), 3.10 (m, *J* = 14.9, 8.8 Hz, 4H), 2.99 (m, 6H), 2.76 (m, *J* = 25.6, 18.5 Hz, 6H), 2.67−2.52 (m, 8H), 1.37−1.35 (m, 18H), 1.25−1.16 (m, 6H). ESI-HRMS: 29/30: $C_{46}H_{73}N_8O_{10}^+$ calcd [M + H]$^+$, 897.5443; measured [M + H]$^+$, 897.5465 (Δ = 2.2 ppm). **31**: ^{1}H NMR (500 MHz, DMSO-d_6): δ 7.97 (d, *J* = 70.8 Hz, 4H), 7.37−7.35 (m, 5H), 5.10 (s, 2H), 3.18−3.13 (m, 4H), 3.09 (m, *J* = 12.6, 6.3 Hz, 6H), 2.99 (m, *J* = 5.6 Hz, 6H), 2.81 (m, *J* = 24.0 Hz, 4H), 2.63 (m, *J* = 4.2 Hz, 4H), 2.59 (m, *J* = 9.7, 7.9 Hz, 4H), 1.36 (s, 33H), 1.20 (d, *J* = 7.0 Hz, 3H). ESI-HRMS: **31**: $C_{47}H_{83}N_{10}O_{11}^+$ calcd [M + H]$^+$, 963.6236; measured [M + H]$^+$, 963.6235 (Δ = 0.1 ppm).

Dibenzyl-2,2′-(4,10-bis((*S*)-1-((2-aminoethyl)amino)-1-oxopropan-2-yl)-1,4,7,10-tetraazacyclododecane-1,7-diyl)-diacetate (32) and Dibenzyl-2,2′-(7,10-bis((*S*)-1-((2-aminoethyl)amino)-1-oxopropan-2-yl)-1,4,7,10-tetraazacyclododecane-1,4-diyl)diacetate (33). **29**/**30** was dissolved in DCM (0.75 mL), and TFA (0.25 mL) was added at 0 °C. Then, the solution was stirred for 1 h at 22 °C. The reaction was concentrated to dryness to afford a mixture **32**/**33** as a white solid (21 mg, 31 μmol, 68%) and employed without further purification in the next step. ESI-HRMS: **32**: $C_{36}H_{57}N_8O_6^+$ calcd [M + H]$^+$, 697.4394; measured [M + H]$^+$, 697.4402 (Δ = 0.8 ppm).

((((((2*S*,2′*S*)-2,2′-(4,10-Bis(2-(benzyloxy)-2-oxoethyl)-1,4,7,10-tetraazacyclododecane-1,7-diyl)bis(propanoyl))bis(azanediyl))bis(ethane-2,1-diyl))bis(azanediyl))bis(carbonyl))-bis(benzene-3,1,2-triyl)tetraacetate (34a) and ((((((2*S*,2′*S*)-2,2′-(7,10-Bis(2-(benzyloxy)-2-oxoethyl)-1,4,7,10-tetraazacyclododecane-1,4-diyl)bis(propanoyl))bis(azanediyl))bis(ethane-2,1-diyl))bis(azanediyl))bis(carbonyl)) bis(benzene-3,1,2-triyl)tetraacetate (35a). To a solution of **2** (7 mg, 31 μmol, 2.2 equiv) in DCM (200 μL) and DMF (50 μL) was added oxalylchloride (5 μL, 62 μmol, 4.4 equiv) at 0 °C, and the solution was stirred for 1 h at 22 °C. The formation of the acid chloride was monitored as previously described. The acid chloride was concentrated under reduced pressure and dried for a minimum of 1 h under high vacuum. A solution of **32**/**33** in $KHCO_3$ (1 M in Milli-Q water, 500 μL) was cooled to 0 °C before the acid chloride was added dropwise in anhydrous 1,4-dioxane (200 μL) while monitoring the pH. The resulting yellow solution was stirred for 30 min at 22 °C, and the solvent was removed by rotary evaporation (water bath: 30 °C). The residue was taken up in MeCN/Milli-Q water (1 mL, 1:1) and purified by RP-HPLC (C18 Phenomenex 40 min gradient, 30−50% MeCN/H_2O, 1% AcOH), and **34a**/**35a** could be obtained as a white solid (12 mg, 11 μmol, 75%). LCMS: *m*/*z* = 1138.35 [M + H$^+$]; t_R = 1.27 min. **34a**/**35a**: ^{1}H NMR (500 MHz, DMSO-d_6): δ 8.39 (m, 3H), 8.16−7.99 (m, 3H), 7.45 (dd, *J* = 7.5, 1.6 Hz, 3H), 7.37−7.35 (m, 16H), 5.09 (s, *J* = 3.8 Hz, 4H), 3.22 (m, 16H), 2.94 (m, 4H), 2.77 (m, 4H), 2.59 (m, 10H), 2.27 (s, 9H), 2.20−2.19 (m, 9H), 1.16 (d, *J* = 5.6 Hz, 6H). ESI-HRMS: **34a**/**35a**: $C_{58}H_{74}N_8O_{16}^{2+}$ calcd [M + 2H]$^{2+}$, 569.2605; measured [M + 2H]$^{2+}$, 569.2586 (Δ = 1.9 ppm).

2,2′-(4,10-Bis((*S*)-1-((2-(2,3-dihydroxybenzamido)ethyl)-amino)-1-oxopropan-2-yl)-1,4,7,10-tetraazacyclododecane-1,7-diyl)diacetic Acid (34) and 2,2′-(7,10-Bis((*S*)-1-((2-(2,3-dihydroxybenzamido)ethyl)amino)-1-oxopropan-2-yl)-1,4,7,10-tetraazacyclododecane-1,4-diyl)diacetic Acid (35). To a solution of **34a** and **35a** (12 mg, 11 μmol, 1.0 equiv) in anhydrous MeOH (0.5 mL) under an Ar atmosphere was added Pd/C (0.3 mg, 0.3 μmol, 0.17 equiv) in dry MeOH (0.5 mL). The reaction was continuously stirred under a H_2 atmosphere for 1.5 h at 25 °C. The reaction was filtered, and the solvent was removed under reduced pressure. The product mixture was purified via RP-HPLC (C18 Phenomenex, 40 min gradient, 10−30% MeCN/H_2O, 0.1% TFA), and **34**/**35** (2.1 mg, 2.7 μmol, 19%) could be obtained as white solids. **34**/**35**: ^{1}H NMR (700 MHz, MeOH-d_4): δ 7.38−7.20 (m, 2H), 6.98−6.86 (m, 2H), 6.77−6.70 (m, 2H), 4.17−3.32 (m, 16H), 3.27−2.82 (m, 14H), 1.34−1.28 (m, 12H) ppm. ESI-HRMS: **34**/**35**: $C_{36}H_{53}N_8O_{12}^+$ calcd [M + H]$^+$, 789.3785; measured [M + H]$^+$, 789.3790 (Δ = 0.5 ppm).

Benzyl-2-(4,7,10-tris((*S*)-1-((2-aminoethyl)amino)-1-oxopropan-2-yl)-1,4,7,10-tetraazacyclododecan-1-yl)acetate (36). To a suspension of **31** (7 mg, 8 μmol, 1.0 equiv) and K_2CO_3 (5 mg, 36 μmol, 4.4 equiv) in MeCN (0.3 mL) was added *o*-benzyl bromoacetate (12 μL, 18 μmol, 2.2 equiv) in MeCN (0.2 mL). The reaction was stirred for 1 h at 22 °C. After completion, the

https://doi.org/10.1021/acs.jmedchem.1c01054
J. Med. Chem. 2021, 64, 12359−12378

reaction was filtered and concentrated to dryness under reduced pressure. The residue was taken up in DCM (0.75 mL), and TFA (0.25 mL) was added at 0 °C. The reaction was stirred for 1 h at 22 °C, then the solvent was removed by rotary evaporation, and **36** could be obtained as a crude, white solid (1.7 mg, 3 μmol, 32%). ESI-HRMS: **36**: $C_{32}H_{59}N_{10}O_5^+$ calcd $[M + H]^+$, 663.4670; measured $[M + H]^+$, 663.4665 (Δ = 0.5 ppm).

2-(4,7,10-Tris((*S*)-1-((2-aminoethyl)amino)-1-oxopropan-2-yl)-1,4,7,10-tetraazacyclododecan-1-yl)acetic Acid (37a). To a solution of **36** (6.4 mg, 10 μmol, 1.0 equiv) in dry MeOH (0.5 mL) under an argon atmosphere was added Pd/C (0.2 mg, 1.7 μmol, 0.17 equiv) in anhydrous, degassed MeOH (0.5 mL). The reaction was continuously stirred under a H_2 atmosphere for 1 h at 22 °C. The suspension was filtered, and product **37a** was obtained after concentration by rotary evaporation (6 mg, 10 μM, quant.) and was directly used in the next step without further purification. ESI-HRMS: 37a: $C_{25}H_{53}N_{10}O_5^+$ calcd $[M + H]^+$, 573.4202; measured $[M + H]^+$, 573.4199 (Δ = 0.3 ppm).

2-(4,7,10-Tris((*S*)-1-((2-(2,3-bis(benzyloxy)benzamido)-ethyl)amino)-1-oxopropan-2-yl)-1,4,7,10-tetraazacyclododecan-1-yl)acetic Acid (37b). To a solution of **2** (6 mg, 11 μmol, 3.3 equiv) in DCM (200 μL) and DMF (50 μL) was added oxalylchloride (3 μL, 35 μmol, 6.6 equiv) at 0 °C, and the reaction was continuously stirred at 22 °C for 1 h. The formation of the acid chloride was monitored as previously described. After removal of the solvent, the acid chloride was dried under high vacuum for a minimum of 1 h. A solution of the amine **37a** (3 mg, 5 μmol, 1.0 equiv) in $KHCO_3$ (1 M in Milli-Q water, 0.5 mL) was cooled to 0 °C before the addition of acid chloride in 1,4-dioxane (0.1 mL), while the pH value was monitored closely. The obtained yellow solution was continuously stirred for 30 min at 22 °C and was concentrated under reduced pressure. Compound **37b** was HPLC-purified (C18 Phenomenex, 40 min gradient, 40−70% MeCN/H_2O, 1% AcOH) and white solid **37b** could be obtained (2.5 mg, 2.03 μmol, 19%). ^{1}H NMR (500 MHz, MeCN-d_3): δ 8.08 (s, 2H), 7.84−7.77 (br s, 2H), 7.77−7.73 (br s, 1H), 7.67−7.59 (br s, 3H), 7.54 (m, 3H), 7.30 (m, 6H), 3.51−3.46 (br s, 2H), 3.45−3.33 (m, 10H), 3.26−3.03 (m, 12H), 2.90−2.77 (br s, 3H), 2.67−2.57 (br s, 8H), 2.26 (s, 9H), 2.24 (s, 3H), 2.23 ppm (s, 6H). ^{13}C NMR (176 MHz, MeCN-d_3): δ 171.8, 169.8, 169.7, 169.5, 169.4, 166.3, 166.3, 163.0, 144.4, 141.6, 141.6, 140.8, 131.9, 131.7, 127.6, 127.5, 127.4, 127.3, 126.8, 126.6, 62.4, 62.2, 59.2, 57.9, 54.5, 52.8, 51.7, 49.5, 41.3, 40.6, 39.9, 39.7, 21.0, 20.9, 20.9, 20.8 ppm.

2-(4,7,10-Tris((*S*)-1-((2-(2,3-dihydroxybenzamido)ethyl)-amino)-1-oxopropan-2-yl)-1,4,7,10-tetraazacyclododecan-1-yl)acetic Acid (37). To a solution of **37b** (2.5 mg, 2.03 μmol, 1.0 equiv) in dry MeOH (0.8 mL), DIPEA (0.2 mL) was added, and the reaction was continuously stirred for 2 h at 22 °C. The mixture was filtrated over a syringe filter, and the eluate was HPLC-purified (C18 Phenomenex, 40 min gradient, 5−35% MeCN/H_2O, 0.1% TFA). Product-containing fractions were identified by LCMS and lyophilized to yield product **37** (0.9 mg, 0.9 μmol, 56%) as a white solid. LCMS: m/z = 491.24 $[M/2 + H^+]$; t_R = 0.86 min. ^{1}H NMR (500 MHz, DMSO-d_6): δ 8.22 (m, 2H), 7.60−7.31 (m, 4H), 6.86 (m, 2H), 6.66−6.56 (m, 6H), 3.41−3.36 (m, 10H), 3.17 (m, 10H), 2.91−2.84 (m, 10H), 2.65 (m, 10H), 1.19 (d, J = 6.4 Hz, 9H) ppm. ESI-HRMS: $C_{46}H_{66}N_{10}O_{14}^{2+}$ calcd $[M + 2H]^{2+}$, 491.2410; measured $[M + 2H]^{2+}$, 491.2376 (Δ = 3.4 ppm).

■ ASSOCIATED CONTENT

Supporting Information

The Supporting Information is available free of charge at https://pubs.acs.org/doi/10.1021/acs.jmedchem.1c01054.

Chemical synthesis, biological experiments, radiochemical procedures, animal experiments, and assay tree for compound design and selection (PDF)

Accumulation of [^{68}Ga]**7** at the infection site (ZIP)

Accumulation of [^{68}Ga]**15** at the infection site (ZIP)

■ AUTHOR INFORMATION

Corresponding Authors

Tobias L. Ross − *Department of Nuclear Medicine, Hannover Medical School, 30625 Hannover, Germany*; Email: Ross.Tobias@mh-hannover.de

Mark Brönstrup − *Department of Chemical Biology, Helmholtz Centre for Infection Research, 38124 Braunschweig, Germany; German Center for Infection Research (DZIF), 38124 Braunschweig, Germany; Center for Biomolecular Drug Research (BMWZ), 30167 Hannover, Germany*; orcid.org/0000-0002-8971-7045; Email: Mark.Broenstrup@helmholtz-hzi.de

Authors

Carsten Peukert − *Department of Chemical Biology, Helmholtz Centre for Infection Research, 38124 Braunschweig, Germany*

Laura N. B. Langer − *Department of Nuclear Medicine, Hannover Medical School, 30625 Hannover, Germany*

Sophie M. Wegener − *Department of Nuclear Medicine, Hannover Medical School, 30625 Hannover, Germany*

Anna Tutov − *Department of Chemical Biology, Helmholtz Centre for Infection Research, 38124 Braunschweig, Germany*

Jens P. Bankstahl − *Department of Nuclear Medicine, Hannover Medical School, 30625 Hannover, Germany*

Bianka Karge − *Department of Chemical Biology, Helmholtz Centre for Infection Research, 38124 Braunschweig, Germany*

Frank M. Bengel − *Department of Nuclear Medicine, Hannover Medical School, 30625 Hannover, Germany*

Complete contact information is available at: https://pubs.acs.org/10.1021/acs.jmedchem.1c01054

Author Contributions

C.P. and L.N.B.L. contributed equally to this publication. All authors analyzed the results, participated in the final revision of the manuscript, and gave final approval for publication.

Funding

The presented work was supported by a "Kekulé-Stipendium" of the "Fonds der chemischen Industrie (VCI)", as well as with a grant from the Joint Programming Initiative on Antimicrobial Resistance (JPI AMR, grant number: 01KI1825).

Notes

The authors declare no competing financial interest.

All animal experiments were conducted according to the German animal welfare law (animal experiment application no. 15-2418), as well as the guide lines of the European parliament in order to protect the animals used for scientific studies (2010/63/EU).

■ ACKNOWLEDGMENTS

We thank Anja Sanders, Petra Felsch, Nele Hermann, and Aylina Glasenapp for their help with animal experiments. We also thank Dr. Annika Heß for preparation of the cryo-sections, and Zekiye Korkmaz for her support with bacterial cultures, as well as Dr. Kevin Ferreira for his support on DOTAM synthesis. Furthermore, we thank Ulrike Beutling for the measurement of HRMS samples and Christel Kakoschke for the measurement of NMR samples.

■ ABBREVIATIONS

BCN-DOTA, 2,2′,2″-(10-(4-((2-((((1*R*,8*S*,9*s*)-bicyclo[6.1.0]-non-4-yn-9-ylmethoxy)carbonyl)amino)ethyl)amino)-1-car-

boxy-4-oxobutyl)-1,4,7,10-tetraazacyclododecane-1,4,7-triyl)-triacetic acid; DOTA, 2,2′,2″,2‴-(1,4,7,10-tetraazacyclododecane-1,4,7,10-tetrayl)tetraacetic acid; DOTAM, 1,4,7,10-tetraazacyclododecane-1,4,7,10-tetraacetic amide; ENT, enterobactin; PYO, pyoverdine; RCP, radiochemical purity; RCY, radiochemical yield; SPAAC, strain-promoted azide−alkyne cycloaddition

REFERENCES

(1) Interagency coordination group on antimicrobial resistance. No time to wait: Securing the future from drug-resistant infections. https://www.who.int/docs/default-source/documents/no-time-to-wait-securing-the-future-from-drug-resistant-infections-en.pdf?sfvrsn=5b424d7_6 (accessed 2021-07-29).

(2) Theuretzbacher, U.; Gottwalt, S.; Beyer, P.; Butler, M.; Czaplewski, L.; Lienhardt, C.; Moja, L.; Paul, M.; Paulin, S.; Rex, J. H.; Silver, L. L.; Spigelman, M.; Thwaites, G. E.; Paccaud, J.-P.; Harbarth, S. Analysis of the clinical antibacterial and antituberculosis pipeline. *Lancet Infect. Dis.* **2019**, *19*, e40−e50.

(3) Tacconelli, E.; Carrara, E.; Savoldi, A.; Harbarth, S.; Mendelson, M.; Monnet, D. L.; Pulcini, C.; Kahlmeter, G.; Kluytmans, J.; Carmeli, Y.; Ouellette, M.; Outterson, K.; Patel, J.; Cavaleri, M.; Cox, E. M.; Houchens, C. R.; Grayson, M. L.; Hansen, P.; Singh, N.; Theuretzbacher, U.; Magrini, N.; Aboderin, A. O.; Al-Abri, S. S.; Awang Jalil, N.; Benzonana, N.; Bhattacharya, S.; Brink, A. J.; Burkert, F. R.; Cars, O.; Cornaglia, G.; Dyar, O. J.; Friedrich, A. W.; Gales, A. C.; Gandra, S.; Giske, C. G.; Goff, D. A.; Goossens, H.; Gottlieb, T.; Guzman Blanco, M.; Hryniewicz, W.; Kattula, D.; Jinks, T.; Kanj, S. S.; Kerr, L.; Kieny, M.-P.; Kim, Y. S.; Kozlov, R. S.; Labarca, J.; Laxminarayan, R.; Leder, K.; Leibovici, L.; Levy-Hara, G.; Littman, J.; Malhotra-Kumar, S.; Manchanda, V.; Moja, L.; Ndoye, B.; Pan, A.; Paterson, D. L.; Paul, M.; Qiu, H.; Ramon-Pardo, P.; Rodríguez-Baño, J.; Sanguinetti, M.; Sengupta, S.; Sharland, M.; Si-Mehand, M.; Silver, L. L.; Song, W.; Steinbakk, M.; Thomsen, J.; Thwaites, G. E.; van der Meer, J. W.; Van Kinh, N.; Vega, S.; Villegas, M. V.; Wechsler-Fördös, A.; Wertheim, H. F. L.; Wesangula, E.; Woodford, N.; Yilmaz, F. O.; Zorzet, A. Discovery, research, and development of new antibiotics: the WHO priority list of antibiotic-resistant bacteria and tuberculosis. *Lancet Infect. Dis.* **2018**, *18*, 318−327.

(4) Mota, F.; Ordonez, A. A.; Firth, G.; Ruiz-Bedoya, C. A.; Ma, M. T.; Jain, S. K. Radiotracer development for bacterial imaging. *J. Med. Chem.* **2020**, *63*, 1964−1977.

(5) Wang, X.; Murthy, N. Bacterial imaging comes of age. *Sci. Transl. Med.* **2014**, *6*, 243−259.

(6) Palestro, C. J.; Love, C.; Miller, T. T. Diagnostic imaging tests and microbial infections. *Cell. Microbiol.* **2007**, *9*, 2323−2333.

(7) Zhuang, H.; Alavi, A. 18-Fluorodeoxyglucose positron emission tomographic imaging in the detection and monitoring of infection and inflammation. *Semin. Nucl. Med.* **2002**, *32*, 47−59.

(8) Fletcher, J. W.; Djulbegovic, B.; Soares, H. P.; Siegel, B. A.; Lowe, V. J.; Lyman, G. H.; Coleman, R. E.; Wahl, R.; Paschold, J. C.; Avril, N.; Einhorn, L. H.; Suh, W. W.; Samson, D.; Delbeke, D.; Gorman, M.; Shields, A. F. Recommendations on the use of 18F-FDG PET in oncology. *J. Nucl. Med.* **2008**, *49*, 480−508.

(9) Sollini, M.; Lauri, C.; Boni, R.; Lazzeri, E.; Erba, P. A.; Signore, A. Current status of molecular imaging in infections. *Curr. Pharm. Des.* **2018**, *24*, 754−771.

(10) Li, J.; Zheng, H.; Fodah, R.; Warawa, J. M.; Ng, C. K. Validation of 2-(18)F-fluorodeoxysorbitol as a potential radiopharmaceutical for imaging bacterial infection in the lung. *J. Nucl. Med.* **2018**, *59*, 134−139.

(11) Weinstein, E. A.; Ordonez, A. A.; DeMarco, V. P.; Murawski, A. M.; Pokkali, S.; MacDonald, E. M.; Klunk, M.; Mease, R. C.; Pomper, M. G.; Jain, S. K. Imaging enterobacteriaceae infection in vivo with 18F-fluorodeoxysorbitol positron emission tomography. *Sci. Transl. Med.* **2014**, *6*, 259ra146.

(12) Martínez, M. E.; Kiyono, Y.; Noriki, S.; Inai, K.; Mandap, K. S.; Kobayashi, M.; Mori, T.; Tokunaga, Y.; Tiwari, V. N.; Okazawa, H.; Fujibayashi, Y.; Ido, T. New radiosynthesis of 2-deoxy-2-[18F]-fluoroacetamido-d-glucopyranose and its evaluation as a bacterial infections imaging agent. *Nucl. Med. Biol.* **2011**, *38*, 807−817.

(13) Ferenci, T. The recognition of maltodextrins by Escherichia coli. *Eur. J. Biochem.* **1980**, *108*, 631−636.

(14) Jones, S. A.; Jorgensen, M.; Chowdhury, F. Z.; Rodgers, R.; Hartline, J.; Leatham, M. P.; Struve, C.; Krogfelt, K. A.; Cohen, P. S.; Conway, T. Glycogen and maltose utilization by Escherichia coli O157:H7 in the mouse intestine. *Infect. Immun.* **2008**, *76*, 2531.

(15) Shelburne, S. A.; Sumby, P.; Sitkiewicz, I.; Okorafor, N.; Granville, C.; Patel, P.; Voyich, J.; Hull, R.; DeLeo, F. R.; Musser, J. M. Maltodextrin utilization plays a key role in the ability of group A Streptococcus to colonize the oropharynx. *Infect. Immun.* **2006**, *74*, 4605−4614.

(16) Axer, A.; Hermann, S.; Kehr, G.; Clases, D.; Karst, U.; Fischer-Riepe, L.; Roth, J.; Fobker, M.; Schäfers, M.; Gilmour, R.; Faust, A. Harnessing the maltodextrin transport mechanism for targeted bacterial imaging: Structural requirements for improved in vivo stability in tracer design. *ChemMedChem* **2018**, *13*, 241−250.

(17) Ning, X.; Lee, S.; Wang, Z.; Kim, D.; Stubblefield, B.; Gilbert, E.; Murthy, N. Maltodextrin-based imaging probes detect bacteria in vivo with high sensitivity and specificity. *Nat. Mater.* **2011**, *10*, 602−607.

(18) Ning, X.; Seo, W.; Lee, S.; Takemiya, K.; Rafi, M.; Feng, X.; Weiss, D.; Wang, X.; Williams, L.; Camp, V. M.; Eugene, M.; Taylor, W. R.; Goodman, M.; Murthy, N. PET imaging of bacterial infections with fluorine-18-labeled maltohexaose. *Angew. Chem., Int. Ed. Engl.* **2014**, *53*, 14096−14101.

(19) Bunschoten, A.; Welling, M. M.; Termaat, M. F.; Sathekge, M.; van Leeuwen, F. W. B. Development and prospects of dedicated tracers for the molecular imaging of bacterial infections. *Bioconjugate Chem.* **2013**, *24*, 1971−1989.

(20) Zhang, Z.; Ordonez, A. A.; Wang, H.; Li, Y.; Gogarty, K. R.; Weinstein, E. A.; Daryaee, F.; Merino, J.; Yoon, G. E.; Kalinda, A. S.; Mease, R. C.; Iuliano, J. N.; Smith-Jones, P. M.; Jain, S. K.; Tonge, P. J. Positron emission tomography imaging with 2-[18F]F-p-amino-benzoic acid detects Staphylococcus aureus infections and monitors drug response. *ACS Infect. Dis.* **2018**, *4*, 1635−1644.

(21) El-ghany, E. A.; Amin, A. M.; El-kawy, O. A.; Amin, M. Technetium-99m labeling and freeze-dried kit formulation of levofloxacin (L-Flox): a novel agent for detecting sites of infection. *J. Labelled Compd. Radiopharm.* **2007**, *50*, 25−31.

(22) Palestro, C.; Love, C.; Caprioli, R.; Marwin, S.; Richardson, H.; Haight, J.; Tronco, G.; Pugliese, P.; Bhargava, K. Phase II study of 99mTc-ciprofloxacin uptake in patients with high suspicion of osteomyelitis. *J. Nucl. Med.* **2006**, *47*, 152.

(23) Essouissi, I.; Darghoutha, F.; Saied, N. M.; Saidi, M.; Kanoun, A.; Saidi, M. Radiolabeling, quality control, and biodistribution of 99mTc-sulfadiazine as an infection imaging agent. *Radiochemistry* **2015**, *57*, 307−311.

(24) le Roux, J.; Rubow, S.; Ebenhan, T.; Wagener, C. An automated synthesis method for 68Ga-labelled ubiquicidin 29−41. *J. Radioanal. Nucl. Chem.* **2020**, *323*, 105−116.

(25) Renick, P. J.; Mulgaonkar, A.; Co, C. M.; Wu, C.-Y.; Zhou, N.; Velazquez, A.; Pennington, J.; Sherwood, A.; Dong, H.; Castellino, L.; Öz, O. K.; Tang, L.; Sun, X. Imaging of actively proliferating bacterial infections by targeting the bacterial metabolic footprint with d-[5-11C]-glutamine. *ACS Infect. Dis.* **2021**, *7*, 347−361.

(26) Holden, V. I.; Bachman, M. A. Diverging roles of bacterial siderophores during infection. *Metallomics* **2015**, *7*, 986−995.

(27) Welling, M. M.; Hensbergen, A. W.; Bunschoten, A.; Velders, A. H.; Roestenberg, M.; van Leeuwen, F. W. B. An update on radiotracer development for molecular imaging of bacterial infections. *Clin. Transl. Imaging* **2019**, *7*, 105−124.

(28) Petrik, M.; Haas, H.; Laverman, P.; Schrettl, M.; Franssen, G. M.; Blatzer, M.; Decristoforo, C. 68Ga-triacetylfusarinine C and 68Ga-ferrioxamine E for Aspergillus infection imaging: uptake specificity in various microorganisms. *Mol. Imag. Biol.* **2014**, *16*, 102−108.

(29) Petrik, M.; Umlaufova, E.; Raclavsky, V.; Palyzova, A.; Havlicek, V.; Haas, H.; Novy, Z.; Dolezal, D.; Hajduch, M.; Decristoforo, C. Imaging of Pseudomonas aeruginosa infection with Ga-68 labelled pyoverdine for positron emission tomography. *Sci. Rep.* **2018**, *8*, 15698.
(30) Petrik, M.; Umlaufova, E.; Raclavsky, V.; Palyzova, A.; Havlicek, V.; Pfister, J.; Mair, C.; Novy, Z.; Popper, M.; Hajduch, M.; Decristoforo, C. (68)Ga-labelled desferrioxamine-B for bacterial infection imaging. *Eur. J. Nucl. Med. Mol. Imag.* **2021**, *48*, 372−382.
(31) Klahn, P.; Brönstrup, M. Bifunctional antimicrobial conjugates and hybrid antimicrobials. *Nat. Prod. Rep.* **2017**, *34*, 832−885.
(32) Wu, J. Y.; Srinivas, P.; Pogue, J. M. Cefiderocol: A novel agent for the management of multidrug-resistant Gram-negative organisms. *Infect. Dis. Ther.* **2020**, *9*, 17−40.
(33) Ferreira, K.; Hu, H.-Y.; Fetz, V.; Prochnow, H.; Rais, B.; Müller, P. P.; Brönstrup, M. Multivalent siderophore−DOTAM conjugates as theranostics for imaging and treatment of cacterial infections. *Angew. Chem., Int. Ed.* **2017**, *56*, 8272−8276.
(34) Stasiuk, G. J.; Long, N. J. The ubiquitous DOTA and its derivatives: The impact of 1,4,7,10-tetraazacyclododecane-1,4,7,10-tetraacetic acid on biomedical imaging. *Chem. Commun.* **2013**, *49*, 2732−2746.
(35) Kubícek, V.; Havlícková, J.; Kotek, J.; Tircsó, G.; Hermann, P.; Tóth, E.; Lukes, I. Gallium(III) complexes of DOTA and DOTA-monoamide: kinetic and thermodynamic studies. *Inorg. Chem.* **2010**, *49*, 10960−10969.
(36) Aime, S.; Botta, M.; Garda, Z.; Kucera, B. E.; Tircso, G.; Young, V. G.; Woods, M. Properties, solution state behavior, and crystal structures of chelates of DOTMA. *Inorg. Chem.* **2011**, *50*, 7955−7965.
(37) Ji, C.; Miller, P. A.; Miller, M. J. Iron transport-mediated drug delivery: Practical syntheses and in vitro antibacterial studies of tris-catecholate siderophore−aminopenicillin conjugates reveals selectively potent antipseudomonal activity. *J. Am. Chem. Soc.* **2012**, *134*, 9898−9901.
(38) Aime, S.; Botta, M.; Ermondi, G. NMR study of solution structures and dynamics of lanthanide(III) complexes of DOTA. *Inorg. Chem.* **1992**, *31*, 4291−4299.
(39) Broan, C. J.; Cox, J. P. L.; Craig, A. S.; Kataky, R.; Parker, D.; Harrison, A.; Randall, A. M.; Ferguson, G. Structure and solution stability of indium and gallium complexes of 1,4,7-triazacyclononanetriacetate and of yttrium complexes of 1,4,7,10-tetraazacyclododecanetetraacetate and related ligands: kinetically stable complexes for use in imaging and radioimmunotherapy. X-Ray molecular structure of the indium and gallium complexes of 1,4,7-triazacyclononane-1,4,7-triacetic acid. *J. Chem. Soc., Perkin Trans.* **1991**, *2*, 87−99.
(40) Desreux, J. F. Nuclear magnetic resonance spectroscopy of lanthanide complexes with a tetraacetic tetraaza macrocycle. Unusual conformation properties. *Inorg. Chem.* **1980**, *19*, 1319−1324.
(41) Keire, D. A.; Kobayashi, M. NMR studies of the metal-loading kinetics and acid−base chemistry of DOTA and butylamide-DOTA. *Bioconjugate Chem.* **1999**, *10*, 454−463.
(42) McCutchan, E. A. Nuclear data sheets for A = 68. *Nucl. Data Sheets* **2012**, *113*, 1735−1870.
(43) Miethke, M.; Marahiel, M. A. Siderophore-based iron acquisition and pathogen control. *Microbiol. Mol. Biol. Rev.* **2007**, *71*, 413−451.
(44) Hider, R. C.; Kong, X. Chemistry and biology of siderophores. *Nat. Prod. Rep.* **2010**, *27*, 637−657.
(45) Harrington, J. M.; Crumbliss, A. L. The redox hypothesis in siderophore-mediated iron uptake. *BioMetals* **2009**, *22*, 679−689.
(46) Lin, H.; Fischbach, M. A.; Liu, D. R.; Walsh, C. T. In vitro characterization of salmochelin and enterobactin trilactone hydrolases IroD, IroE, and Fes. *J. Am. Chem. Soc.* **2005**, *127*, 11075−11084.
(47) Coenen, H. H.; Gee, A. D.; Adam, M.; Antoni, G.; Cutler, C. S.; Fujibayashi, Y.; Jeong, J. M.; Mach, R. H.; Mindt, T. L.; Pike, V. W.; Windhorst, A. D. Open letter to journal editors on: International consensus radiochemistry nomenclature guidelines. *Ann. Nucl. Med.* **2018**, *32*, 236−238.
(48) Joaqui-Joaqui, M. A.; Pandey, M. K.; Bansal, A.; Raju, M. V. R.; Armstrong-Pavlik, F.; Dundar, A.; Wong, H. L.; DeGrado, T. R.; Pierre, V. C. Catechol-based functionalizable ligands for gallium-68 positron emission tomography imaging. *Inorg. Chem.* **2020**, *59*, 12025−12038.
(49) Tsionou, M. I.; Knapp, C. E.; Foley, C. A.; Munteanu, C. R.; Cakebread, A.; Imberti, C.; Eykyn, T. R.; Young, J. D.; Paterson, B. M.; Blower, P. J.; Ma, M. T. Comparison of macrocyclic and acyclic chelators for gallium-68 radiolabelling. *RSC Adv.* **2017**, *7*, 49586−49599.
(50) Wright, C. I. The enzymatic deacetylation of heroin and related morphine derivatives by blood serum. *J. Pharmacol. Exp. Therapeut.* **1941**, *71*, 164−177.
(51) Bahar, F. G.; Ohura, K.; Ogihara, T.; Imai, T. Species difference of esterase expression and hydrolase activity in plasma. *J. Pharm. Sci.* **2012**, *101*, 3979−3988.
(52) Velikyan, I.; Antoni, G.; Sörensen, J.; Estrada, S. Organ biodistribution of Germanium-68 in rat in the presence and absence of [(68)Ga]Ga-DOTA-TOC for the extrapolation to the human organ and whole-body radiation dosimetry. *Am. J. Nucl. Med. Mol. Imaging* **2013**, *3*, 154−165.
(53) Finberg, K. E. Ironing out an approach to alleviate the hypoferremia of acute inflammation. *Haematologica* **2021**, *106*, 326−328.
(54) Sheldon, J. R.; Heinrichs, D. E. Recent developments in understanding the iron acquisition strategies of Gram-positive pathogens. *FEMS Microbiol. Rev.* **2015**, *39*, 592−630.
(55) Moynié, L.; Milenkovic, S.; Mislin, G. L. A.; Gasser, V.; Malloci, G.; Baco, E.; McCaughan, R. P.; Page, M. G. P.; Schalk, I. J.; Ceccarelli, M.; Naismith, J. H. The complex of ferric-enterobactin with its transporter from Pseudomonas aeruginosa suggests a two-site model. *Nat. Commun.* **2019**, *10*, 3673.
(56) Usher, K. C.; Özkan, E.; Gardner, K. H.; Deisenhofer, J. The plug domain of FepA, a TonB-dependent transport protein from Escherichia coli, binds its siderophore in the absence of the transmembrane barrel domain. *Proc. Natl. Acad. Sci. U.S.A.* **2001**, *98*, 10676−10681.
(57) Kumar, A.; Chakravorty, S.; Yang, T.; Majumdar, A.; Newton, S.; Klebba, P. Fluorescence spectroscopic analysis of TonB-dependent transport in Klebsiella pneumoniae. *FASEB J.* **2019**, *33*, 635.12.
(58) Rabsch, W.; Winkelmann, G. n. The specificity of bacterial siderophore receptors probed by bioassays. *Biol. Met.* **1991**, *4*, 244−250.
(59) Heppeler, A.; Froidevaux, S.; Mäcke, H. R.; Jermann, E.; Béhé, M.; Powell, P.; Hennig, M. Radiometal-labelled macrocyclic chelator-derivatised somatostatin analogue with superb tumour-targeting properties and potential for receptor-mediated internal radiotherapy. *Chem.—Eur. J.* **1999**, *5*, 1974−1981.
(60) Clarke, E. T.; Martell, A. E. Stabilities of the Fe(III), Ga(III) and In(III) chelates of N,N′,N″-triazacyclononanetriacetic acid. *Inorg. Chim. Acta* **1991**, *181*, 273−280.
(61) André, J. P.; Maecke, H. R.; André, J. P.; Zehnder, M.; Macko, L.; Akyel, K. G. 1,4,7-Triazacyclononane-1-succinic acid-4,7-diacetic acid (NODASA): a new bifunctional chelator for radio gallium-labelling of biomolecules. *Chem. Commun.* **1998**, *12*, 1301−1302.
(62) Singh, A. N.; Liu, W.; Hao, G.; Kumar, A.; Gupta, A.; Öz, O. K.; Hsieh, J.-T.; Sun, X. Multivalent bifunctional chelator scaffolds for gallium-68 based positron emission tomography imaging probe design: Signal amplification via multivalency. *Bioconjugate Chem.* **2011**, *22*, 1650−1662.
(63) Kriemen, E.; Holzapfel, M.; Ruf, E.; Rehbein, J.; Maison, W. Synthesis and structural analysis of 1,4,7,10-tetraazacyclododecane-1,4,7,10-tetraazidoethylacetic acid (DOTAZA) complexes. *Eur. J. Inorg. Chem.* **2015**, *2015*, 5368−5378.
(64) Mao, J.; Liu, F.; Wang, M.; Wu, L.; Zheng, B.; Liu, S.; Zhong, J.; Bian, Q.; Walsh, P. J. Cobalt−bisoxazoline-catalyzed asymmetric kumada cross-coupling of racemic α-bromo esters with aryl grignard reagents. *J. Am. Chem. Soc.* **2014**, *136*, 17662−17668.

https://doi.org/10.1021/acs.jmedchem.1c01054
J. Med. Chem. 2021, 64, 12359−12378

(65) Moore, T. W.; Sana, K.; Yan, D.; Thepchatri, P.; Ndungu, J. M.; Saindane, M. T.; Lockwood, M. A.; Natchus, M. G.; Liotta, D. C.; Plemper, R. K.; Snyder, J. P.; Sun, A. Asymmetric synthesis of host-directed inhibitors of myxoviruses. *Beilstein J. Org. Chem.* **2013**, *9*, 197−203.

https://doi.org/10.1021/acs.jmedchem.1c01054
J. Med. Chem. 2021, 64, 12359−12378